

Winter intrusions of Atlantic Water in Kongsfjorden: oceanic preconditioning and atmospheric triggering

Francesco De Rovere¹, Davide Zanchettin², Angelo Rubino³, Leonardo Langone⁴, Francesco Calogiuri⁵, Paolo Ruggieri⁶, Angelo Lupi⁴, and Jacopo Chiggiato⁷

¹Ca' Foscari University of Venice

²University Ca'Foscari of Venice

³Università Ca' Foscari di Venezia

⁴Consiglio Nazionale delle Ricerche - Istituto di Scienze Polari

⁵University of Bologna

⁶University of L'Aquila

⁷CONSIGLIO NAZIONALE DELLE RICERCHE

June 23, 2023

Abstract

Kongsfjorden is an Arctic fjord in Svalbard, which is largely influenced by the West Spitsbergen Current (WSC), transporting warm and salty Atlantic Water (AW) into the Arctic. The geostrophic control typically prevents AW from entering the fjord in winter, whereas energetic wind events develop the Spitsbergen Trough Current (STC), ultimately flooding fjords facing the West Spitsbergen Shelf with AW. However, an exhaustive understanding of the interplay between these two opposite mechanisms and a clear knowledge of conditions leading to AW winter intrusions are still lacking. In this study, observational and reanalysis data show that wind reversal events trigger AW intrusions, while the ocean density is a key preconditioning factor limiting the occurrence of AW intrusions to specific winters only. Wind reversals are strong southerly wind events linked to the setup of a high pressure anomaly over the Barents Sea, followed by a circulation reversal with northerly winds. Winters with AW intrusions feature fresher and less dense fjord waters compared to AW, resulting in the breakdown of the geostrophic control mechanism at the fjord mouth, which opens the fjord to waters advected from the WSC by wind reversals. The low salinity signal is consistent with a large freshwater production through summer Arctic sea-ice melting in the Barents Sea. Another mechanism is observed only in winter 2014: southern winds blew continuously for two months and transported surface AW from the WSC to the fjord, eventually forcing AW to intrude near the surface, on top of denser local waters.

Hosted file

964968_0_art_file_11094010_rwvrq0.docx available at <https://authorea.com/users/630743/articles/650400-winter-intrusions-of-atlantic-water-in-kongsfjorden-oceanic-preconditioning-and-atmospheric-triggering>

Hosted file

964968_0_supp_11069367_rvx22b.docx available at <https://authorea.com/users/630743/articles/650400-winter-intrusions-of-atlantic-water-in-kongsfjorden-oceanic-preconditioning-and-atmospheric-triggering>

1 **Winter intrusions of Atlantic Water in Kongsfjorden: oceanic**
2 **preconditioning and atmospheric triggering**

3
4 **Francesco De Rovere^{1,2}, Davide Zanchettin¹, Angelo Rubino¹, Leonardo Langone²,**
5 **Francesco Calogiuri³, Paolo Ruggieri³, Angelo Lupi², Jacopo Chiggiato⁴**

6
7 ¹ Department of Environmental Sciences, Informatics and Statistics, Ca' Foscari University of
8 Venice, Venezia, Italy

9 ² Consiglio Nazionale delle Ricerche, Istituto di Scienze Polari (CNR-ISP), Bologna, Italy

10 ³ Department of Physics and Astronomy, University of Bologna, Bologna, Italy

11 ⁴ Consiglio Nazionale delle Ricerche, Istituto di Scienze Marine (CNR-ISMAR), Venezia, Italy

12
13 **Key points:**

- 14 • Sudden intrusions of Atlantic Water in Kongsfjorden during winter are triggered by
15 abrupt reversals of local meridional winds
- 16 • The geostrophic control is disrupted by the advection of anomalously low salinity
17 waters in the fjord, opening the fjord to AW intrusions
- 18 • The 2014 Atlantic Water intrusion was triggered by long-lasting southerly winds,
19 transporting warm surface waters toward the fjord

20 Plain Language Summary

21 Kongsfjorden is an Arctic fjord in Svalbard, which is largely influenced by the West
22 Spitsbergen Current (WSC), transporting warm and salty Atlantic Water (AW) into the Arctic.
23 In the fjord, occasional winter intrusions of AW occur, leading to abrupt warming events. We
24 found that such intrusions are triggered by wind reversals, i.e., energetic winds from the
25 south followed by winds from the north, which uplift AW from the WSC and guide it toward
26 Kongsfjorden. However, AW can enter the fjord only in those winters characterized by a fjord
27 density lower than that of the WSC, which typically follows a large freshwater production
28 through summer Arctic sea-ice melting in the Barents Sea. Hence, the atmosphere initially
29 triggers the AW intrusion, while ocean conditions defining each winter are a key
30 preconditioning factor opening the fjord to the intrusion. A second mechanism is observed
31 only in 2014: winds from the south blew continuously for two months and transported surface
32 AW from the WSC to the fjord, eventually forcing AW to intrude near the surface, on top of
33 denser local waters.

34

35

36 Abstract

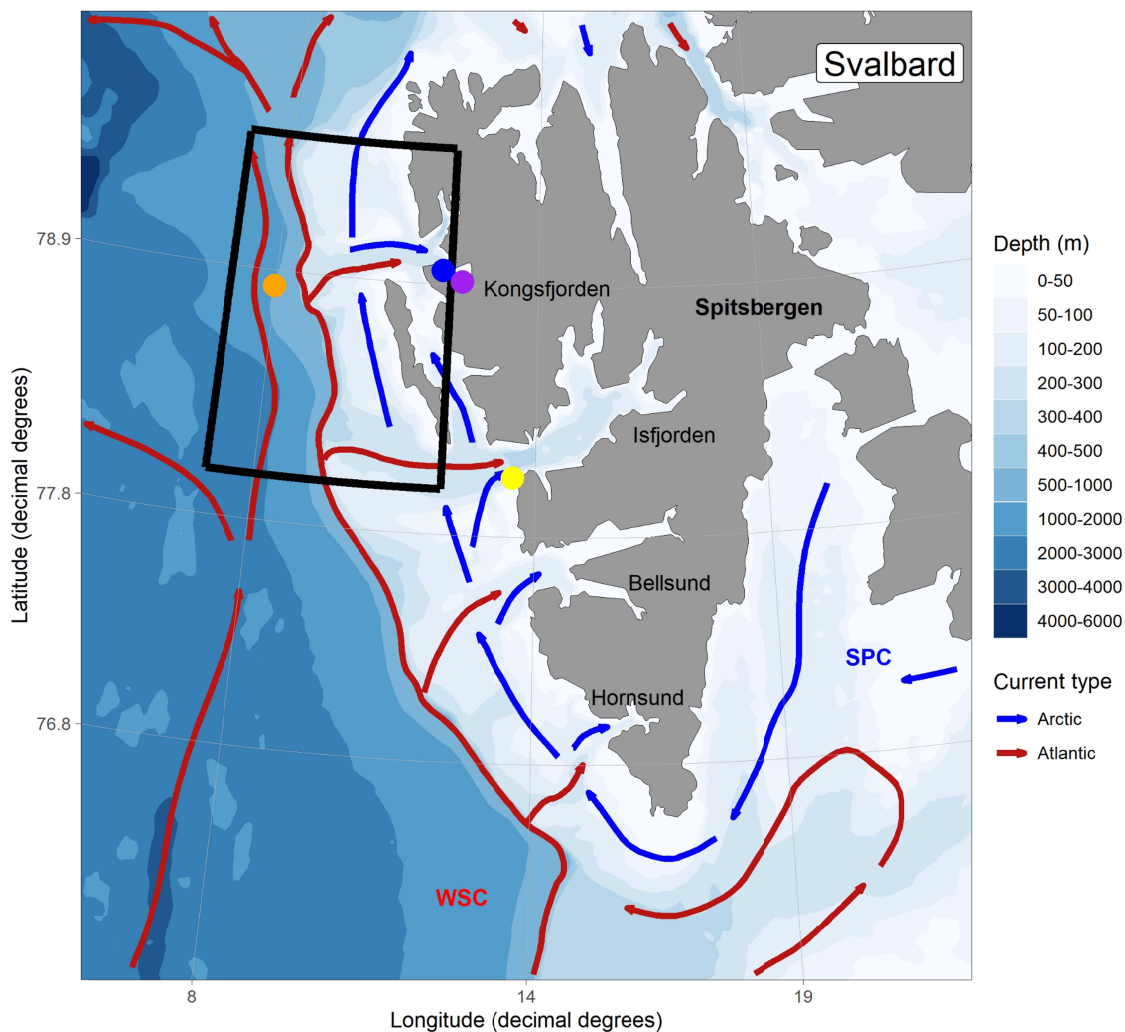
37 Kongsfjorden is an Arctic fjord in Svalbard, which is largely influenced by the West
38 Spitsbergen Current (WSC), transporting warm and salty Atlantic Water (AW) into the Arctic.
39 The geostrophic control typically prevents AW from entering the fjord in winter, whereas
40 energetic wind events develop the Spitsbergen Trough Current (STC), ultimately flooding
41 fjords facing the West Spitsbergen Shelf with AW. However, an exhaustive understanding of
42 the interplay between these two opposite mechanisms and a clear knowledge of conditions
43 leading to AW winter intrusions are still lacking. In this study, observational and reanalysis
44 data show that wind *reversal* events trigger AW intrusions, while the ocean density is a key
45 preconditioning factor limiting the occurrence of AW intrusions to specific winters only. Wind
46 *reversals* are strong southerly wind events linked to the setup of a high pressure anomaly
47 over the Barents Sea, followed by a circulation reversal with northerly winds. Winters with
48 AW intrusions feature fresher and less dense fjord waters compared to AW, resulting in the
49 breakdown of the geostrophic control mechanism at the fjord mouth, which opens the fjord to
50 waters advected from the WSC by wind *reversals*. The low salinity signal is consistent with a
51 large freshwater production through summer Arctic sea-ice melting in the Barents Sea.
52 Another mechanism is observed only in winter 2014: southern winds blew continuously for
53 two months and transported surface AW from the WSC to the fjord, eventually forcing AW to
54 intrude near the surface, on top of denser local waters.

55 1. Introduction

56 The Arctic is acknowledged as a “climatic hotspot” by the scientific community (Meredith et
57 al., 2019). Arctic surface temperatures are increasing at a higher rate compared to the global
58 average since the 1960s, a process named *Arctic amplification* (Chylek et al., 2009; Serreze
59 & Barry, 2011; Richter-Menge and Druckenmiller, 2020), sustaining the loss of Arctic sea-ice
60 volume (Carmack et al., 2015; Comiso, 2012) and the *ice-albedo feedback* (Curry et al.,
61 1995). The Eurasian Arctic is subjected to *Atlantification*, i.e., the propagation of the Atlantic
62 domain toward the Arctic (Lind et al., 2018; Polyakov et al., 2017). The stability of the water
63 column, featuring fresh and cold Arctic Water (ArW) on top and warmer and saltier Atlantic
64 Water (AW) at intermediate/deep layers is being eroded by an enhanced upward flux of heat
65 and salt. Principal consequences are sea-ice melting, warming of the lower atmosphere, a
66 change in air-ocean interactions and in the ecosystem structure (Ingvaldsen et al., 2021).

67 The Svalbard archipelago is set in the Eurasian Arctic and surrounds the eastern side of the
68 Fram Strait, the main gateway of AW to the central Arctic basin. The largest island, i.e.,
69 Spitsbergen, presents different broad fjords on its western side: Kongsfjorden, Isfjorden,
70 Bellsund and Hornsund. The hydrography and climate of these fjords are largely influenced
71 by the two main currents of the region: the West Spitsbergen Current (WSC) and the
72 Spitsbergen Polar Current (SPC) (Helland-Hansen & Nansen, 1909). The barotropic and
73 topographically steered WSC transports AW northward along the continental slope. The
74 WSC is characterized by a strong seasonality, with the largest AW transport in late autumn
75 and early winter (Beszczynska-Möller et al., 2012b; Walczowski & Piechura, 2011). WSC
76 properties and structure undergo large interannual variability linked to the general oceanic
77 and atmospheric circulation pattern over the North Atlantic (Chatterjee et al., 2018; Muilwijk
78 et al., 2018; Raj et al., 2018; Wang et al., 2020). The SPC flows northward on the West
79 Spitsbergen Shelf (WSS), parallelly to the WSC, and is identified by cross-shelf sloping
80 isopycnals, revealing its geostrophic nature (Svendsen et al., 2002). It carries ArW and sea-
81 ice from Storfjorden and the Barents Sea, and travels on the shallowest layers close to the
82 West Spitsbergen coast. Figure 1 illustrates a map of Spitsbergen and its fjords, along with
83 main currents flowing in the area.

84



85

86 Figure 1: Map of West Spitsbergen with main Arctic (blue) and Atlantic (red) water currents.

87 The four coloured points represent the location of the 4 moorings whose observations are

88 used in this study: MDI (purple), KF (blue), I1 (yellow) and F3 (orange). The black box

89 indicates the area A1, where ERA5 atmospheric wind data are evaluated. The color scale

90 illustrates the bathymetry. This figure has been generated through the PlotSvalbard R

91 package (Vihtakari, 2020).

92

93 Kongsfjorden (Hop and Wiencke, 2019) is the northernmost broad fjord in West Spitsbergen,

94 and is connected with WSC waters through a deep trough, Kongsfjordrenna. In the fjord,

95 occasional winter intrusions of AW occur, leading to large positive temperature and salinity

96 anomalies. AW in Kongsfjorden is defined by Tverberg et al. (2019) as water with $T > 3^{\circ}\text{C}$

97 and salinities larger than 34.9. ArW instead is defined as Local Water (LW) and indicates

98 those waters with $T < 1^{\circ}\text{C}$. Variable dilutions between LW and AW take the form of

99 Intermediate Water and Transformed Atlantic Water. Different mechanisms have been
100 proposed to explain AW intrusions in Kongsfjorden. A geostrophic control mechanism
101 prevents shelf waters from entering the fjord, especially during the winter season (Cottier et
102 al., 2005; Klinck et al., 1981; Svendsen et al., 2002). The degree of control is determined by
103 the strength of the SPC, depending primarily on the shelf-fjord density gradient. When the
104 coastal current faces larger densities on the right, i.e., when the density in the fjord is larger
105 than that on the shelf, its strength will increase with increasing depths. This condition is
106 typical of winter months when fjord heat loss to the atmosphere and sea-ice production
107 increase density in the deep fjord basin. As a result, AW advected near the bottom through
108 Kongsfjordrenna will join this current at the fjord mouth, making a detour northward. On the
109 opposite, when shelf waters are denser than fjord waters, typically in summer months, during
110 which large amounts of freshwaters are released from local glaciers, the speed of the
111 coastal current will decrease with depth. The geostrophic control mechanism breaks down
112 and WSC waters are free to enter the fjord at intermediate and large depths, while the
113 coastal current is confined in the upper layers. Density variations on the shelf develop
114 horizontal pressure gradients between the fjord and the shelf driving baroclinic currents
115 (Klinck et al., 1981; Stigebrandt et al., 1981; Svendsen et al., 1980). Such variations are
116 generated by wind convergence and divergence near the coast, causing downwelling and
117 upwelling, or by advection of horizontal density gradients along the coast. Strong southerly
118 winds and a negative wind curl over the WSS can stack up less dense surface waters along
119 the coast. Once the wind ceases, the water column on the shelf returns to a normal
120 stratification state and the fjord adjusts to it with an outflow near the surface and an inflow
121 near the bottom. Episodes of this “intermediary circulation” have been observed also in
122 Greenland fjords (Jackson et al., 2014; Straneo et al., 2010). Wind events on the shelf can
123 also lead to geostrophic advection of WSC waters into West Spitsbergen fjords through the
124 development of the Spitsbergen Through Current (STC) (Nilsen et al., 2016). Water
125 convergence near the coast enhances the positive gradient in the surface tilt over the shelf
126 break. As a result, both the WSC and the SPC are strengthened (Teigen et al., 2010), and
127 the WSC is moved on shallower isobaths on the WSS, generating the topographically guided
128 STC. Once the wind turns northerly, upwelling of the STC starts on the shelf. Nilsen et al.
129 (2016) and Cottier et al. (2007) suggest that the resulting offshore surface current on the
130 shelf opposes the SPC and can break down the geostrophic control mechanism, allowing
131 the STC to intrude in West Spitsbergen fjords. The strong southerly wind events described
132 by Nilsen et al. (2016) are the so-called winter cyclones. Strong blocking conditions
133 developing over Scandinavia and Europe stretch the Atlantic storm track over the Greenland
134 Sea to the Arctic, including Svalbard (Häkkinen et al., 2011; Rogers et al., 2005; Ruggieri et
135 al., 2020), generating southerly winds over the eastern Fram Strait and the arrival of warm

136 and humid air masses over Svalbard. Other effective means of shelf-fjord exchanges are
137 instabilities at the WSC-SPC front, developing topographic waves (Nilsen et al., 2006;
138 Teigen et al., 2010, 2011). Stable topographic waves are generated by wind events at the
139 shelf-edge front and can develop coastally trapped waves traveling along isobaths on the
140 steep southern side of Kongsfjordrenna (Inall et al., 2015).

141 *Atlantification* is leaving its footprint on West Spitsbergen fjords by increasing their water
142 temperatures and salinities (Bloskhina et al., 2021; Cottier et al., 2019; De Rovere et al.,
143 2022; Skogseth et al., 2020; Strzelewicz et al., 2022; Tverberg, et al., 2019). After 2006,
144 winters became more Atlantic-like with no sea ice and occasional shallow AW advection
145 (Tverberg et al., 2019). Furthermore, the occurrence of intense winter cyclones passing over
146 Svalbard in winter is increasing (Zahn et al., 2018), potentially boosting winter AW advection
147 on the WSS and adjacent fjords. An increasing heat content in the fjord affects also the
148 stability of ecosystem's structure (Hegseth and Tverberg, 2013; Payne and Roesler, 2019;
149 Vihtakari et al., 2018) and tidewater glaciers (Holmes et al., 2019; Luckman et al., 2015).

150 Henceforth, the dynamics of AW winter intrusions should be interpreted to fully understand
151 ongoing changes in Kongsfjorden and its future evolution, especially under the influence of
152 *Atlantification* and *Arctic amplification*. To the best of our knowledge, a clear examination of
153 AW winter intrusion events in the fjord after the 2006/2007 event is lacking. In addition, there
154 is a need to robustly define common traits, especially the large-scale atmospheric and
155 oceanic settings leading to AW winter intrusions. In particular, the relation and interplay
156 between the two most important mechanisms, i.e., the STC and the geostrophic control
157 mechanism, are not clearly defined. Despite being a very important factor driving dynamics
158 on the WSS, a complete understanding of the SPC's influence on winter water masses
159 variability in Kongsfjorden is still to be defined (Tverberg et al., 2019). The scientific
160 community now has access to *in-situ* continuous measurements acquired over the 2011-
161 2020 decade from several mooring lines in the West Spitsbergen area. Exploiting the
162 availability of such an extensive dataset and high-resolution reanalysis products (ERA5), a
163 deep joint examination of the typical mechanisms leading to AW winter intrusions in
164 Kongsfjorden can now be performed. Oceanographic observations in Kongsfjorden are not
165 just describing current conditions and ongoing changes in the fjord itself, but can be
166 indicators for the other West Spitsbergen fjords as well as for similar shelf-fjord systems in
167 the Arctic.

168 The aim of this work is to investigate winter (January to March) AW intrusions in
169 Kongsfjorden during the 2011-2020 decade by jointly examining local and large-scale
170 atmospheric and oceanic dynamics, combining *in-situ* and reanalyzed observations. The
171 specific objectives are: to give a concise overview of winter AW intrusions occurred in the

172 2011-2020 decade in Kongsfjorden and to assess the dynamics of such events, particularly
173 the large-scale atmospheric and oceanic conditions.

174 This paper is organized as follows: Section 2 provides an overview of the data utilized in this
175 study and the methods for data analysis. Section 3 combines the presentation of the results
176 with a discussion. Section 4 provides a summary and illustrates the main conclusions of this
177 study.

178

179 **2. Data and Methods**

180 2.1 Data

181 2.1.1 In-situ data

182 *In-situ* oceanic observations in Kongsfjorden are retrieved by two mooring lines: MDI and
183 KF. The former is managed by the Institute of Polar Sciences of the National Research
184 Council of Italy (CNR-ISP). MDI is anchored at approximately 105 m depth in inner
185 Kongsfjorden and has been monitoring temperature and salinity at 85 m since September
186 2010 (D'Angelo et al., 2018; De Rovere et al., 2022). KF is located in the mid fjord at
187 approximately 260 m depth, and is managed by the University of Tromso (UiT) in
188 collaboration with the Scottish Association for Marine Sciences (SAMS). Two continuous
189 temperature and salinity records are available from 2006 to 2018, except for 2012, at the
190 near surface (circa 30 m depth) and the near-bottom (circa 230 m depth). KF has also been
191 supplied with several thermistors at different depths, allowing for the representation of
192 temperature along the water column. Furthermore, KF is equipped with two ADCPs
193 providing current data. Ocean current observations are averaged in the vicinity of
194 temperature and salinity sensors, at 20-30 m (near-surface) and 200-210 m (near-bottom)
195 depth, and their tidal frequencies removed. The University Centre in Svalbard (UNIS) is
196 maintaining the I1 mooring, situated in the southern end of Isfjorden's mouth. Temperature
197 and salinity observations at 190 m depth are assessed to depict conditions on the shelf
198 adjacent to Isfjorden. The Alfred Wegener Institute, Helmholtz Center for Polar and Marine
199 Research (AWI) ran a monitoring program composed of a mooring array positioned in the
200 Fram Strait from late 1990s to 2016 (Beszczynska-Möller et al., 2012b). We selected one
201 mooring, i.e, F3, positioned at the shelf break and whose temperature and salinity data
202 collected at 250 m depth describe the properties of the WSC. *In-situ* local atmospheric
203 observations in Kongsfjorden as air temperature, relative humidity and winds, are retrieved
204 from the Climate Change Tower (CCT) located in the village of Ny-Alesund, on the southern
205 side of the fjord.

206

207 2.1.2 Reanalysis datasets

208 Winds at 10 m height and geopotential height fields at 850 hPa over the Arctic and Fram
209 Strait regions are utilized to describe large-scale atmospheric conditions. Data are retrieved
210 from ERA5 reanalyses. Wind and wind curl data are averaged over an area representative of
211 the WSS adjacent to Kongsfjorden (A1, black rectangle reported in Figure 1; 7-12 °E, 78-
212 79.5 °N). We also use salinity fields at 50 m depth from the CMEMS Arctic Ocean Physics
213 Reanalysis to define the large scale oceanic conditions in Svalbard and the Barents Sea.
214 Data regarding the main northern Atlantic hemispheric teleconnection patterns are retrieved
215 from the NOAA Climate Prediction Center and are: the North Atlantic Oscillation, the Arctic

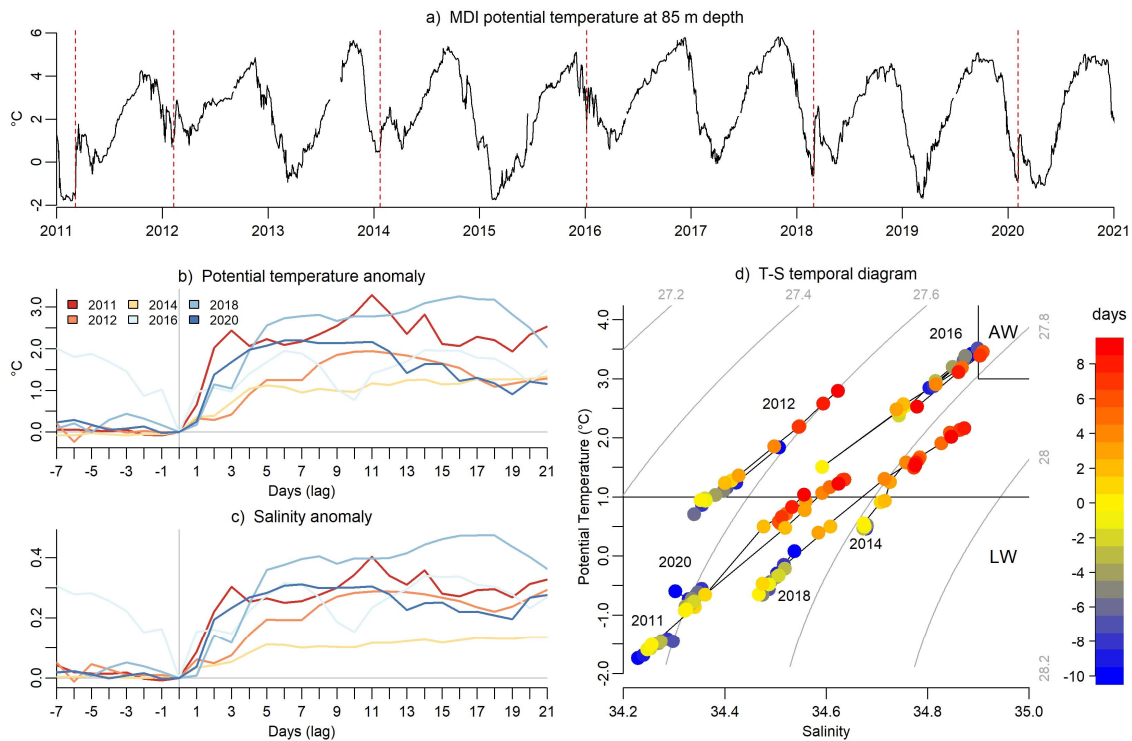
216 Oscillation, the East Atlantic Pattern, the East Atlantic/Western Russia pattern, Scandinavia
217 Pattern.

218

219 2.2 Methods

220 All data were averaged at a daily frequency, except for climate indices. We choose the *onset*
221 *date* ($t = 0$) of AW intrusion events by selecting the time of a large and sudden increase in
222 temperature and salinity in Kongsfjorden *in-situ* oceanic observations from MDI and KF (see
223 Section 3.1 and Figure 2 for more details). We determine the peculiar atmospheric
224 conditions characterizing AW intrusion events through a Superposed Epoch Analysis (SEA)
225 (Chree, 1912; Chree, 1913; Singh, 2006). This technique allows to detect common features
226 shared by target events against background noise. We select the onset dates ($t = 0$) of the
227 AW intrusion and we average conditions over the previous week ($-7 \leq t \leq -1$) and the
228 following week ($0 \leq t \leq 6$). The two weekly means calculated for each event are then
229 averaged into two single averages in the case of punctual time series, or two maps as in the
230 case of two-dimensional atmospheric fields.

231 **3. Results and discussion**
 232 3.1 Definition of Atlantic Water intrusion events
 233



234
 235 Figure 2: Definition of AW intrusion events as from MDI observations. a) Daily averaged
 236 temperature at 85 m depth with dashed red lines indicating the selected onset of AW
 237 intrusion events. b) Potential temperature and c) salinity daily anomaly series at 85 m depth
 238 around the AW intrusions. Anomalies are calculated by subtracting the temperature and
 239 salinity value of the onset day from the two series, respectively. The two series have been
 240 lagged so that the onset of each event corresponds to lag=0. d) T-S diagrams representing
 241 85 m depth observations acquired from day -10 to day +9 for each event.

242
 243 Figure 2a reports the ocean temperature observed by MDI at 85 m depth in inner
 244 Kongsfjorden, from 2011 to late 2020. We identified 6 winter AW intrusion events occurring
 245 in 2011, 2012, 2014, 2016, 2018 and 2020. The events feature large and sudden increases
 246 in water temperature and salinity, as reported in Figure 2b-c. Onset dates (see section 2.2)
 247 are labeled by vertical dashed red lines in Figure 2a and the zero lag vertical line in Figure
 248 2b-c, and are the following: 2011-03-07, 2012-02-11, 2014-02-24, 2016-01-06, 2018-03-01,
 249 2020-02-04. The largest temperature change takes place within the first 5 days from the
 250 onset. In this time range, the greatest temperature growth occurred in 2018 (2.51 °C), while
 251 the lowest in 2014 (1.1 °C). Figure 2d reports a T-S diagram showing the temperature and
 252 salinity evolution in the neighborhood of each event. LW is present in inner Kongsfjorden in

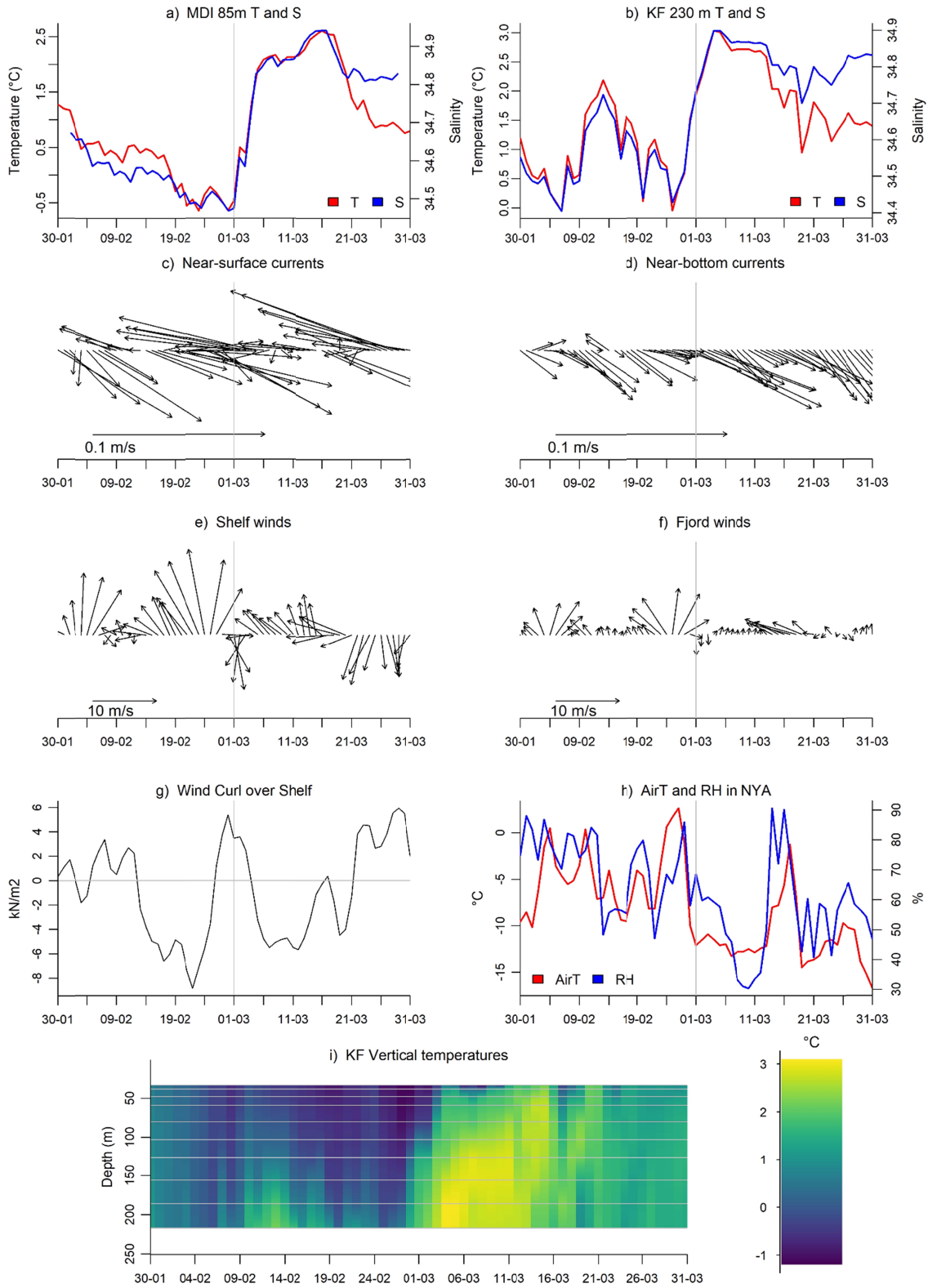
253 the days before the event are then replaced by variable dilutions with AW. This represents a
254 clear signal of an AW intrusion event from the WSC to Kongsfjorden. The winter 2016 event
255 is peculiar since it is not characterized by a single intrusion event but by several short-lived
256 events.

257

258 3.2.1 Mechanism for upwelling events

259 AW intrusions occurred in 2011, 2012, 2016, 2018 and 2020 shared common dynamics,
260 where warmer temperatures propagate from the fjord's bottom toward the surface, in a few
261 days. Winter 2018 is reported in Figure 3 as an emblematic example of these “upwelling”
262 events, while the others are reported in supplementary Figures S1 to S4. In these figures,
263 besides MDI data, we make use of the oceanographic observations from mooring KF, as
264 well as *in-situ* and reanalysis atmospheric data, to examine the local oceanic and
265 atmospheric variability.

266



267

268

269

270

Figure 3: Winter 2018 as representative of upwelling events: temperature and salinity at MDI (a) and KF (b); near-surface (c) and near-bottom (d) currents from KF; average winds (e) and wind stress curl (g) over A1 from ERA5; fjord winds (f) and meteorological conditions (h)

271 from the CCT; (i) KF temperature profile with gray horizontal lines identifying sensors'
272 depths.

273

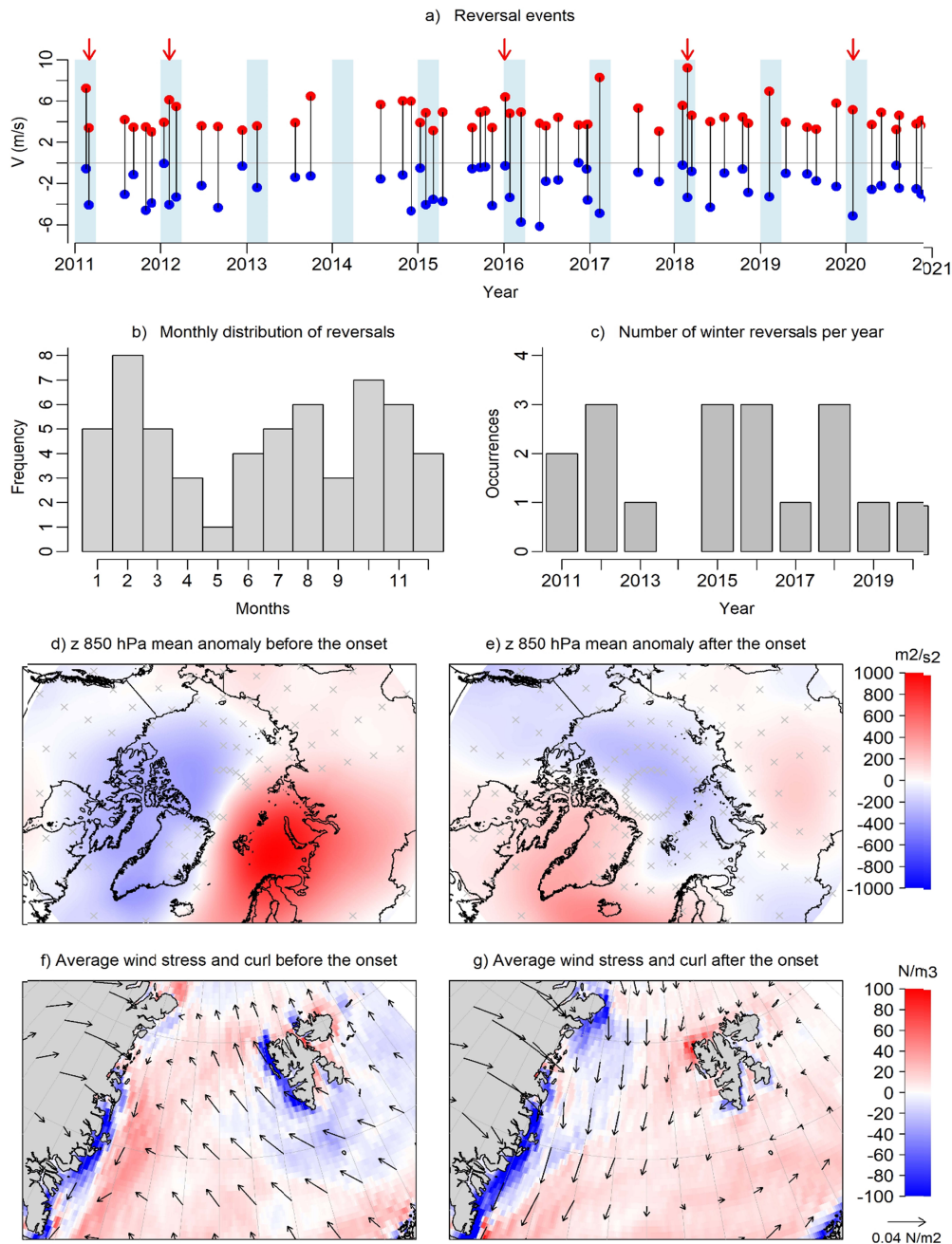
274 The warming signal at KF (Figure 3b) precedes MDI (Figure 3a) by approximately 3-4 days
275 in each intrusion event by upwelling. Another weaker warm water intrusion occurred near
276 mid-February 2018 near the bottom, which does not propagate toward the surface, as it is
277 detected only at 230 m depth and not at 85 m. The AW intrusion is accompanied by large
278 outflowing current velocities near the surface (Figure 3c) and large inflowing current
279 velocities at depth (Figure 3d), both along the main fjord axis. Instead, days preceding the
280 intrusion's *onset* feature inflowing currents near the surface and very low velocities near the
281 bottom. Shelf winds are primarily southerly in the week before the *onset* and then turn
282 northerly in the week after the *onset*. We name these atmospheric events as *reversals*.
283 Winds in the fjord reflect the main evolution observed on the shelf (Figure 3f). Southerlies
284 bring very warm and humid air, rising air temperatures in Kongsfjorden even above zero for
285 some days, then replaced by cold and dry air brought by northerlies after the *onset date*
286 (Figure 3h). The average wind curl is largely negative before the *onset*, turning to positive
287 when KF temperature increases. This atmospheric evolution over the West Spitsbergen area
288 appears to be the key common mechanism triggering upwelling warming events in
289 Kongsfjorden (see also Figure S1 to S4). This dynamic is consistent with the development of
290 the STC on the WSS (Nilsen et al., 2016) and the intermediary circulation between
291 Kongsfjorden and Kongsfjordrenna (Stigebrandt et al., 1981). Southerly winds and the
292 negative wind curl force surface waters to stack up along the West Spitsbergen coast. The
293 resulting increase in the cross-shelf sea surface tilt forces the WSC on shallower isobaths on
294 the shelf, developing the STC. Once southerly winds cease, the sea-surface tilt relaxes and
295 surface waters tend to flow offshore, compensated by an inflow from the shelf break on the
296 lower levels. AW now can flow at the deepest levels on the shelf toward the fjord. Northerly
297 winds further drive surface waters off Kongsfjorden, which are compensated by the inflow of
298 AW from the STC near the bottom. AW is uplifted by upwelling and reaches the near
299 surface.

300

301 3.2.2 Atmospheric triggering: "reversal" events

302 This section examines the occurrence of wind *reversal* events and the associated large-
303 scale atmospheric patterns. We define wind *reversals* as those events featuring strongly
304 southerly winds ($V > 3$ m/s) blowing on the WSS (area A1) in the week before and northerly
305 ($V < 0$ m/s) in the week after the *onset* of AW intrusion events. The occurrence of wind
306 *reversal* events in the 2011-2020 decade, irrespective of their association with an AW

307 intrusion event, as well as the associated large-scale geopotential and wind stress curl
 308 patterns are examined in Figure 4 through ERA5 observations.
 309



310
 311 Figure 4: (a) Average V in the week before (red points) and after (blue points) the *onset* of
 312 *reversals*. Blue areas indicate winter months (Jan-Mar). Monthly (b) and yearly (c) frequency
 313 of *reversals* during the 2011-2020 decade. Average geopotential anomalies at 850 hPa (d,
 314 e), wind stress and wind stress curl (f, g) before and after the onset of *reversals* occurred in
 315 the 2011-2020 decade. Geopotential anomalies are calculated considering the 2011-2020

316 time period as climatology. In Figure 4d-e, areas marked with gray crosses are non-
317 significant anomalies (see Appendix A for a complete description of the significance
318 analysis).

319

320 *Reversal* occur throughout the year and are not confined to the winter season, as reported in
321 Figure 4a-b, with two local maxima in February and October. *Reversals* occurred almost in
322 every winter of the decade, up to three events per season (Figure 4c), for a total of 18 winter
323 events. We further examine *reversal*'s characteristics using this larger pool instead of only
324 the five upwelling events to increase the robustness and significance of our results.

325 Atmospheric conditions before and after the onset of *reversal* events reflect two strongly
326 different large-scale/synoptic circulations. Strong southerly wind events in the week before
327 the onset are generated by the setup of a high pressure anomaly centered over the Barents
328 Sea and a low pressure anomaly over north-eastern Canada and Greenland (Figure 4d).
329 This geopotential dipole sets up strong geostrophic winds blowing from the south over the
330 Fram Strait, moving waters toward the physical barrier represented by the West Spitsbergen
331 coast (Figure 4f). In addition, wind stress curl indicates upwelling in the central Fram Strait
332 and strong downwelling on the WSS, this being driven by the slower winds interacting with
333 the terrain over the Svalbard archipelago. The situation changes suddenly in a few days,
334 from daily southerlies of 10 m/s to northerlies of 6-7 m/s. The restoration of a low pressure
335 anomaly over the north pole (Figure 4e), the Svalbard archipelago and the northern Barents
336 Sea triggers northerly winds initiating upwelling on the WSS (Figure 4g), especially on the
337 northern WSS. Note that these negative geopotential anomalies are not significantly different
338 from typical pressure conditions characterizing winter months. The link of these *reversals*
339 with the general atmospheric circulation is further examined through a correlation analysis
340 between the number of winter reversal events per year and the winter average of several
341 teleconnection indices (see Section 2.1.2). The only significant (p -value=0.01) correlation (-
342 0.4) is found with the Arctic Oscillation (AO). A negative phase of the AO is associated with a
343 weaker jet stream in the northern hemisphere, characterized by large meanders propagating
344 high pressure anomalies as north as the Barents Sea and Fram Strait and negative pressure
345 anomalies toward the mid-latitudes. A negative AO phase can thus set up a pressure
346 anomaly field at high latitudes characterized by large zonal gradients, a feature consistent
347 with the geopotential dipole observed in Figure 5a, hence increasing the probability of large
348 meridional winds over the Fram Strait.

349 In conclusion, *reversals* are common phenomena occurring throughout the decade, and are
350 not associated to just one season and neither to specific years. An important question arises
351 from this observation: why do AW intrusions occur only in some winters and do not follow
352 every *reversal* event? We hypothesize that *reversals* are not the only key aspect initiating

353 AW intrusions, despite they develop the STC and set off the movement of AW toward
354 Kongsfjorden. Another key factor opens and closes the fjord to AW intrusion in specific
355 winters, and this role is played by the ocean.

356

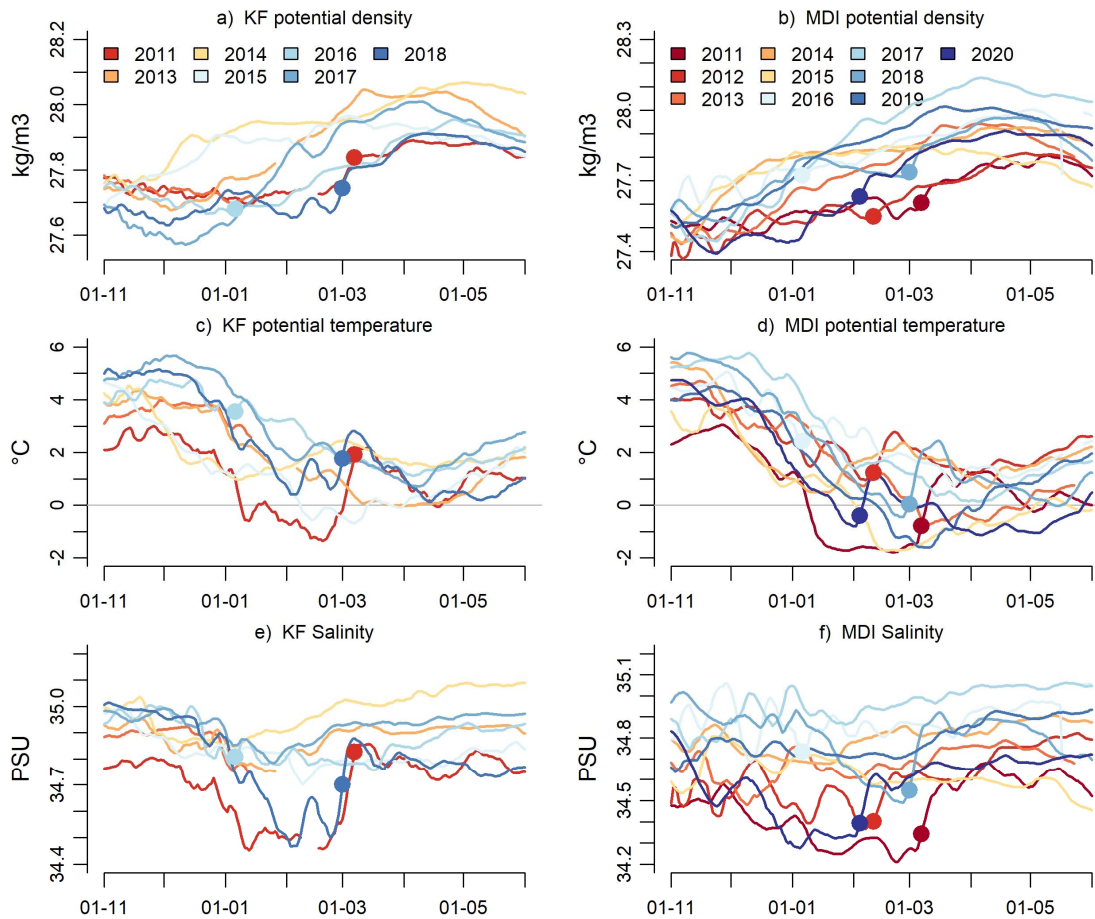
357 3.2.3 Oceanic preconditioning

358 The ocean opens and closes Kongsfjorden to AW intrusions through the geostrophic control
359 (Klinck et al., 1981; Cottier et al., 2005). Here we will demonstrate that this mechanism
360 contributes to explain the inter-annual variability in AW winter intrusions in Kongsfjorden, and
361 how the SPC and large-scale oceanic conditions play a key role in preconditioning the fjord
362 in winter.

363 Figure S5 reports the oceanic conditions in Kongsfjorden in the week before and after the
364 onset of all 2011-2020 winter atmospheric *reversals* from observations acquired by KF and
365 MDI. Three clear features stand out. First, not all *reversals* are followed by a large positive
366 temperature change, as in the case of AW intrusion events by upwelling. Second, the five
367 AW intrusion by upwelling show the largest difference in potential density between fjord
368 bottom waters and inflowing waters (Figure S5a-b), a feature consistent with the disruption
369 of the geostrophic control. Third, the five AW intrusion by upwelling are characterized by low
370 density bottom fjord waters in the week before the *onset*. These low density waters result
371 from the presence of low salinity waters (2011, 2012, 2018, 2020 events) or very warm
372 waters (2016 event). The autumn and winter inter-annual variability in potential density,
373 potential temperature and salinity at KF and MDI is examined in Figure 5.

374

375



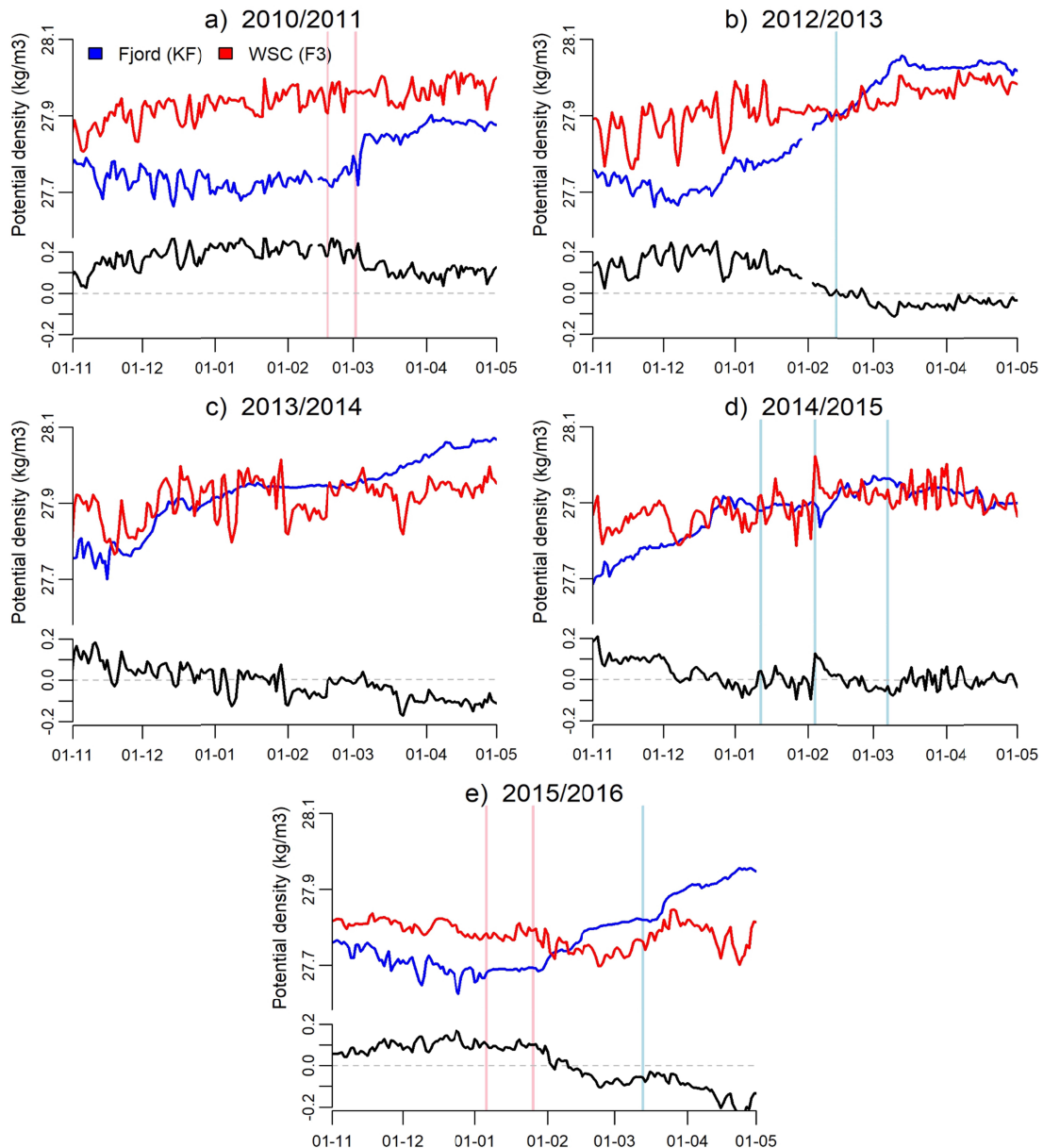
376

377 Figure 5: Potential density (a, b), potential temperature (c, d), salinity (e, f) at KF (230 m) and
 378 MDI (85 m) between November of the previous year and June of the current year (see
 379 legends). Time series are smoothed with a 7-days moving average. Dots indicate the onset
 380 of AW intrusion events at MDI, as identified in section 3.1.

381

382 Figure 5a-b indicates that low density waters are not confined just within the period
 383 preceding the warming, but characterizes the whole winter season of those years with AW
 384 intrusions by upwelling in Kongsfjorden: 2011, 2016 and 2018 for KF (Figure 5a); 2011,
 385 2012, 2018 and 2020 for MDI (Figure 5b). Note here that KF has no measurements for
 386 winters 2012, 2019 and 2020. The low density is linked to the low salinity signal (Figure 5e)
 387 characterizing those winters, apart from 2016. At 230 m depth, salinity in 2011 and 2018
 388 drops right before the beginning of the new year to a local minimum around February. A
 389 similar behaviour is observed for MDI (Figure 5f). Here, low salinities characterize January
 390 and February of those years with AW intrusion by upwelling, i.e., 2011, 2012, 2018 and
 391 2020, even though here in the inner fjord there is not a clear salinity drop as in the mid fjord.
 392 Winter 2016 is a peculiar event as it features several different but frequent AW intrusions

393 events already from the end 2015 (De Rovere et al., 2022), leaving continuous warm and
 394 low density conditions in the mid fjord for the whole winter.
 395 To better understand how this inter-annual variability in near-bottom density influences the
 396 geostrophic control in the winter season, measurements from KF and F3 (WSC at the shelf-
 397 slope) are examined in Figure 6.
 398
 399



400
 401 Figure 6: Potential density at KF (230 m depth, blue lines) and F3 (250 m depth, red lines)
 402 between October and May for those years with simultaneous measurements. Dates of
 403 reversals are represented with vertical blue lines, while vertical red lines identify reversals

404 associated with AW intrusions. The lower side of each panel reports the difference between
405 F3 and KF potential densities.

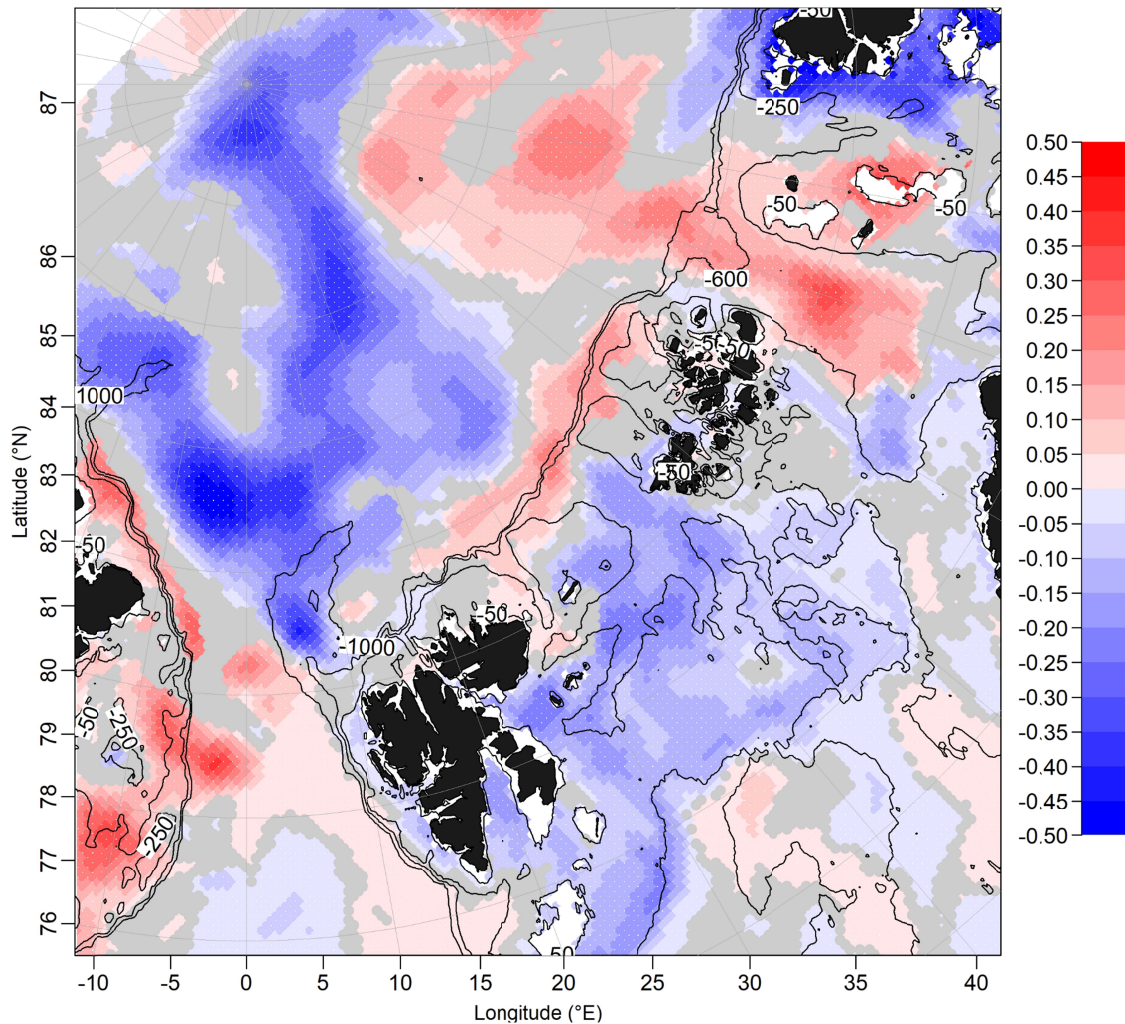
406

407 The potential density of the WSC tends to increase from September to May, except for
408 winter 2016. Fjord density generally grows over the winter season, but the timing of the
409 growth can change from year to year, some in early winter, as 2013, 2014 and 2015, and
410 some other later as 2011 and 2016. This large inter-annual variability in fjord density is a key
411 element affecting the cross-shelf density gradient. *Reversals* occurred in 2011 and 2016
412 found a positive off-shore density gradient (Figure 6a,e), indicating a disrupted geostrophic
413 control, eventually allowing the AW from the STC to flood the fjord. On the contrary,
414 *reversals* occurring in the other winters (Figure 6b,c,d) found a negative off-shore density
415 gradient. This is associated to an active geostrophic control which blocks the AW conveyed
416 by the STC directed toward Kongsfjorden. In this case, northerly winds upwell fjord deep
417 waters.

418 Results indicate that the occurrence of AW winter intrusions in Kongsfjorden is principally
419 linked to winter density conditions, whose inter-annual variability largely depends on the
420 arrival of fresher waters at the fjord near-bottom (2011, 2012, 2018 and 2020). Observations
421 from mooring I1, located on the shelf adjacent to Isfjorden, are investigated to examine the
422 origin of this freshwater signal. Both density and salinity at 160 m depth shows an inter-
423 annual variability consistent with KF and MDI data, featuring lower values during winters
424 characterized by upwelling events (Figure S6). I1 observations also show that winter 2012,
425 which was not recorded by KF, features a low potential density at the beginning of the
426 season, with values comparable to those of 2011 and 2018 winters. Low density waters in
427 years with AW intrusion by upwelling are thus found both in Kongsfjorden and Isfjorden,
428 suggesting a common freshwater source for these two locations. The main freshwater
429 source in winter in the West Spitsbergen area is the SPC, which transport ArW and sea-ice
430 from the Barents Sea through Storfjorden to the WSS. The SPC is thus the primary factor
431 driving the peculiar inter-annual variability in the shelf and fjords' winter density, eventually
432 opening Kongsfjorden to AW winter intrusions once triggered by atmospheric *reversals*. The
433 large-scale salinity conditions in the Eurasian Arctic is examined in Figure 7 to investigate
434 the source of this freshwater signal.

435

Jan-Feb mean salinity difference between winters with and without AW intrusions



436

437 Figure 7: January-February mean salinity difference at 50 m depth between winters with AW
 438 intrusions (2011, 2012, 2018, 2020) and winters with no AW intrusion (2013, 2015, 2017,
 439 2019). Blue (red) areas are characterized by lower (larger) salinities during years with AW
 440 intrusions in Kongsfjorden. Gray areas identify locations whose two daily salinity pools do
 441 not come from two significantly different distributions at the 99% confidence level (see
 442 Appendix B). Data are from the CMEMS daily Arctic Ocean Physics Reanalyses.

443

444

445 Significantly lower salinities in the WSS at 50 m depth are seen for those years featuring an
 446 AW intrusion by upwelling (2011, 2012, 2018, 2020), compared to the other winters (2013,
 447 2015, 2017, 2019). Besides the WSS, this negative salinity anomaly characterizes
 448 Storffjorden and the region south of the Svalbard archipelago, the northern Barents Sea and
 449 the central Arctic basin. We hypothesize this winter large scale salinity structure to be
 450 consistent with a large export of freshwater from strong sea-ice melting during the previous

451 summer season. Indeed, the upper ocean in the northern Barents Sea in winter is very
452 sensitive to the freshwater input from melting sea ice in the previous summer season
453 (Lundesgaard et al., 2022). The region at the edge between the Barents Sea and the central
454 Arctic basin, corresponding roughly to the summer sea-ice transition zone, features a
455 positive salinity anomaly. This could be associated to the absence of large freshwater
456 volumes concentrated in that location as in the other years, or the footprint of larger AW
457 inflows in summer/autumn from the WSC to the area north of Svalbard and the Western
458 Nansen Basin (Duarte et al., 2020), which could intensify sea-ice melting.
459 Another important mechanism which could drive the inter-annual variability in winter density
460 on the WSS and adjacent fjords may be related to the occurrence of extensive AW advection
461 in the previous summer/autumn. As the case of summer/autumn 2016 featuring one of the
462 strongest AW intrusions in Kongsfjorden of the decade (De Rovere et al., 2022), these
463 events may leave a denser water column at the end of the year. Then, the freshwater carried
464 by the SPC in the following months could not be enough by itself to significantly lower the
465 density in the fjord, leaving the geostrophic control at the fjord mouth unaffected.

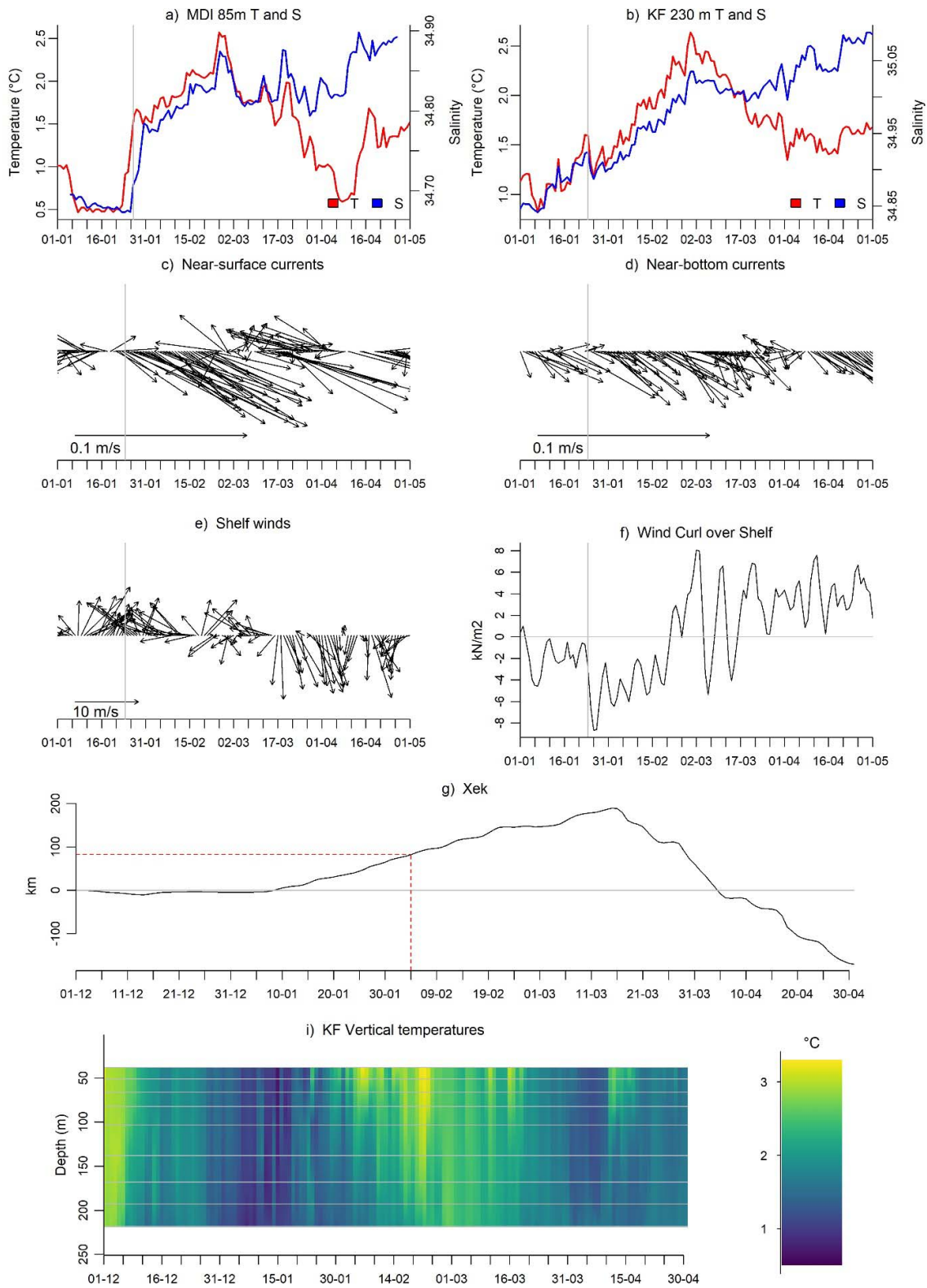
466

467

468 3.3 Downwelling event: 2014

469 The AW intrusion event in 2014 shows a different dynamic compared to the other years, i.e.,
470 through downwelling. Figure 8 reports the main oceanic and atmospheric physical
471 parameters describing the event.

472



473

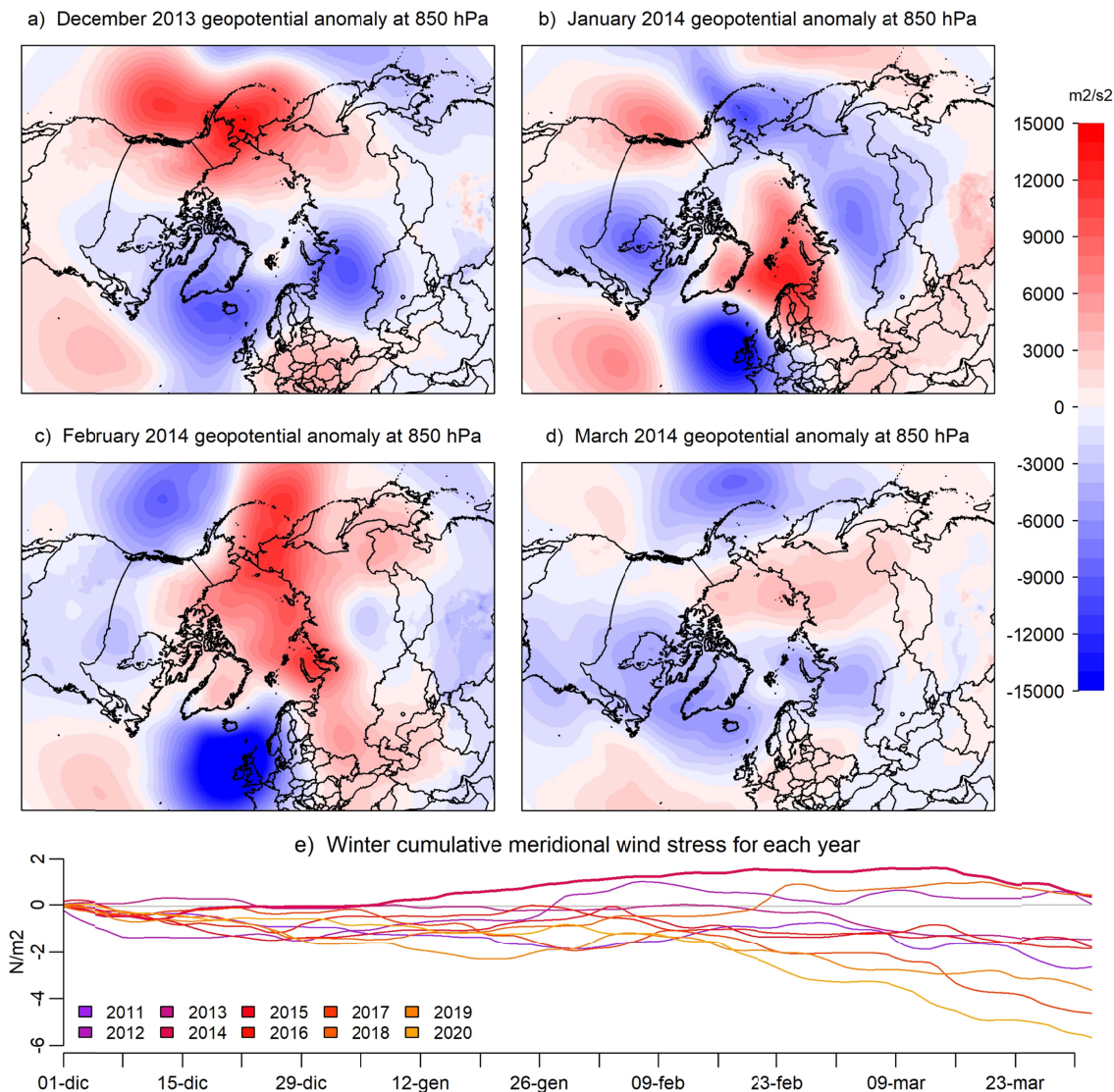
474 Figure 8: Winter 2014 AW intrusion: a) temperature and salinity at MDI; b) temperature and
 475 salinity at KF; c) near-surface currents from KF; d) near-bottom currents from KF; e) average
 476 winds over the shelf (area A1) from ERA5 ; f) average wind curl over the shelf (area A1) from

477 ERA5; g) cumulative net onshore displacement (X_{EK}) calculated using average winds in A1
478 (see appendix C); i) KF temperature profile, gray horizontal lines identify sensors' depths.

479

480 In the downwelling event, warming starts from above and slowly reaches the near-bottom
481 (Figure 8i). Near-bottom sensors at KF experienced a gradual warming and salinification
482 from January to March (Figure 8b), while at mid-depth MDI detected a sudden increase in
483 temperature and salinity (Figure 8a). Currents show inflowing velocities and higher values
484 are seen in the near-surface (Figure 8c) compared to the near-bottom (Figure 8d). Shelf
485 winds have blown almost constantly from the south from the end of January to the end of
486 February (Figure 8e), instaurating downwelling conditions (Figure 8f). Winds in the fjord blew
487 constantly from the south, bringing warm and humid air in Kongsfjorden (not shown). A
488 peculiar difference with the previously described upwelling mechanism is the absence of
489 wind *reversals* in this winter (Figure 4). We hypothesize that long-lasting, constant southerly
490 winds transported the shallowest WSC layers toward the fjord, which were eventually forced
491 to enter on top of fjord waters. The cumulative net onshore displacement (X_{EK} , see appendix
492 C) shows that the theoretical Ekman layer covers the total distance between the shelf break
493 (F3 location), where the WSC flows, and Kongsfjorden (KF location) in 64 days, thus arriving
494 in the fjord at the beginning of February 2014 (see red dashed lines in Figure 8g). This result
495 is in line with the first arrival of warm waters at the near-surface in KF in the same days
496 (Figure 8i). Another critical point in this winter are the properties and the vertical extension of
497 the WSC at the shelf break. 2014 is the second warmest winter at 70 m depth as well as the
498 winter with the highest temperature difference between 70 and 250 m depth, according to 13
499 years of F3 measurements from 1999 to 2015 (Figure S7). This indicate that the core of the
500 WSC is shallower in winter 2014 compared to the other years, and warm waters could have
501 been more easily transported toward the coast of Spitsbergen. Figure 9 illustrates the
502 specific atmospheric conditions of winter 2014.

503



504

505 Figure 9: Atmospheric conditions in winter 2014. Mean geopotential anomaly at 850 hPa in
 506 December 2013 (a), January 2014 (b), February 2014 (c) and March 2014 (d). Climatology is
 507 computed over the 2011-2020 decade. (e) Cumulative meridional wind stress from
 508 December to April for winters in the 2011-2020 decade.

509

510 A strong positive geopotential anomaly centered in the Barents Sea develops in January
 511 2014 (Figure 9b) and persists in February 2014 (Figure 9c), while a strong negative
 512 geopotential anomaly develops in the north-eastern Atlantic region, between Iceland and
 513 Great Britain. This particular atmospheric setting is similar to the one observed for upwelling
 514 events (Figure 4d), with an important difference. Indeed, this persistent positive geopotential
 515 anomaly generates southerly winds over the Fram Strait almost continuously for two months,
 516 as also reported by Figure 9e. Here, winter 2014 (thicker purple line) has a continuous

517 positive meridional wind stress, reaching the highest positive cumulative values of the
518 decade.

519 **4. Summary and Conclusions**

520 This paper examines the mechanisms of AW winter intrusions in Kongsfjorden through
521 continuous mooring observations as well as atmospheric and oceanic reanalysis products.
522 AW winter intrusions in the 2011-2020 decade are relatively common events, leading to a
523 temperature and density increase of at least 1°C and 0.03 kg/m³, respectively, in just a few
524 days, and leaving a warmer and denser water column for a few weeks. Five events took
525 place in winters 2011, 2012, 2016, 2018 and 2020 by means of upwelling. Intrusions are
526 activated by energetic wind *reversal* events blowing over the WSS, causing strong southerly
527 winds and downwelling conditions, followed by northerly winds and upwelling conditions.
528 According to Nilsen et al. (2016), *reversals* move WSC waters on the shallower isobaths on
529 the WSS, setting up the STC transporting AW toward Kongsfjorden. Southerlies are
530 developed by the setup of a strong pressure dipole, with a high pressure center over the
531 Barents Sea and a low pressure center over Greenland and Northern Canada. Afterwards,
532 northerly winds are generated by the restoration of the normal low pressure conditions over
533 the Central Arctic and the Svalbard archipelago. The occurrence of winter *reversal* events is
534 significantly correlated to the mean winter AO conditions. Accordingly, the large meanders in
535 the jet stream associated with the negative AO phase are more likely to trigger the
536 geopotential dipole associated with atmospheric *reversals*. *Reversals* occurred almost every
537 winter in the 2011-2020 decade, and thus are not the only key aspect driving AW intrusions.
538 The ocean is a crucial preconditioning factor, limiting intrusions only to those winters
539 characterized by a negative on-shore density gradient, i.e., when fjord waters are less dense
540 than WSC waters, which disrupts the geostrophic control mechanism (Cottier et al., 2005).
541 That is the case of all winters with AW intrusions by upwelling, where low density bottom
542 waters in the fjord are linked to the external advection of fresher (2011, 2012, 2018, 2020) or
543 warmer (2016) waters before the *onset* of the intrusion. We identified the SPC as the key
544 driver of the freshwater input, which transport anomalously low salinity waters from the
545 northern Barents Sea to the WSS, produced by the melting of large Arctic sea-ice volumes in
546 the previous summer. We foreseen the Arctic sea-ice melting cycle to drive the variability in
547 the SPC properties, which eventually freshens the WSS in some winters and allow the
548 development of AW intrusions by upwelling. Instead, the warmer conditions seen in 2016 are
549 the footprint of an extensive AW intrusion occurred in the second half of 2015. Winter 2014
550 AW intrusion occurred by means of downwelling, driven by the particular atmospheric
551 pattern and oceanic conditions characterizing this winter. On the WSS, southerly winds have
552 blown almost continuously during January and February, transporting waters from the top
553 layers of the WSC toward Kongsfjorden. AW then intruded on top of fjord waters. Southerly
554 winds have been induced by the set up of a long-lasting high pressure anomaly over the

555 Barents Sea and the Eurasian Arctic region, which contrasted a low pressure anomaly over
556 the north-eastern Atlantic Ocean.

557 The different AW intrusion mechanisms examined in this study relates to the winter
558 scenarios proposed by Tverberg et al. (2019), which link the character of the winter AW
559 intrusion in Kongsfjorden to the water column's structure in the following summer. The
560 upwelling mechanism is consistent with the *Winter Intermediate* scenario, where the AW
561 intrusion occurs at depth and, depending on the magnitude of the upwelling, it can reach the
562 fjord surface. Differently, the downwelling mechanism is consistent with the *Winter Open*
563 scenario, where the AW intrudes on top of fjord waters and spreads toward the bottom, likely
564 by cooling and densification. Finally, those winters characterized by the absence of an AW
565 intrusion are consistent with the *Winter Deep* scenario, where the fjord's water column
566 undergoes convection and densification, closing the fjord to the AW. Here, the larger fjord
567 densities are also benefiting from the extensive AW intrusion occurring in the previous
568 autumn season, leaving a saltier water column.

569 This study improved the understanding of winter AW intrusion mechanics by discussing the
570 dynamical aspects of two types of AW intrusion events. The emerging picture shows that
571 both the atmospheric and oceanic components are relevant in determining the timing and
572 inter-annual variability of upwelling events and, more generally, of Kongsfjorden's winter
573 conditions. Indeed, winters characterized by a negative AO phase and following a summer
574 with intense sea-ice melting have a very high chance to see the occurrence of an AW
575 intrusion. Furthermore, the SPC is revealed to play a critical role by transmitting the low
576 density signal from the northern Barents Sea over the WSS to the adjacent fjords. Given the
577 uttermost importance of the SPC for AW intrusions in Kongsfjorden, future studies should
578 focus on describing its seasonal and interannual variability, as well as identify the most
579 important factors regulating its properties.

580 **Acknowledgements**

581 ADCP and CTD data for mooring KF were provided by the Kongsfjorden Rijpfjorden
582 Observatory Program (KROP) which has been supported by the UK Natural Environment
583 Research Council (Oceans 2025 and Northern Sea Program) and the Research Council of
584 Norway (projects Cleopatra: 178766, Cleopatra II: 216537, Circa: 214271/ F20, Marine
585 Night: 26471, FAABulous: 243702, ArcticABC: 244319 and Deep Impact: 300333). We
586 would like to acknowledge the UNIS courses AB-320 and AB-321 for the cooperation in the
587 use of ship time.

588 We thank Daniel Ludwig Vogedes for sharing the ADCP data for KF.

589

590 **Open research**

591 MDI and CCT data (CNR – National Research Council of Italy, 2022) can be found in the
592 Italian Arctic Data Center at https://data.iadc.cnr.it/erddap/files/mdi_ctd_timeseries_1/.
593 KF temperature and salinity data (Cottier et al., 2021a, 2021b, 2021c; Cottier et al., 2022a,
594 2022b, 2022,c, 2022d, 2022e, 2022f, 2022g, 2022h, 2022i) can be found in the NIRD
595 research data archive (<archive.sigma2.no/>). KF raw ADCP data can be requested to
596 daniel.vogedes@uit.no and will be updated in the NIRD research data archive.
597 F3 data (Beszczynska-Möller et al., 2012a, 2015; von Appen et al., 2015, 2017) can be
598 found in the PANGAEA data archive (doi.org/10.1594/PANGAEA.900883).
599 I1 data (Skogseth and Ellingsen, 2019a, 2019b, 2019c, 2019d, 2019e, 2019f, 2019g, 2019h)
600 can be found at the Norwegian Polar Data Centre (data.npolar.no/home/).
601 ERA5 data (Hersbach et al., 2023a, 2023b) are available from the Copernicus program at
602 doi.org/10.24381/cds.adbb2d47 for hourly data on single levels and at
603 doi.org/10.24381/cds.bd0915c6 for hourly data on pressure levels.
604 CMEMS Arctic Ocean Physics Reanalysis data (CMEMS – Copernicus Marine Service,
605 2022) are available from the E.U. Copernicus Marine Service Information at
606 doi.org/10.48670/moi-00007.

607

608 **Appendixes**

609 Appendix A: Significance analysis for Figure 4d and 4e

610 Figure 4d,e are an average of the geopotential anomalies observed in the week before and
 611 after the onset of *reversals* occurred in winters over the 2011-2020 decade, for a total of 18
 612 events. We assess the significance of these mean anomalies as follows: 18 casual dates
 613 over 2011-2020 winters are selected as *onsets*. The associated mean geopotential
 614 anomalies of the week before and after these 18 casual dates are calculated. We repeat this
 615 step 100 times to produce a distribution of geopotential mean anomalies observed in the
 616 week before and after casual dates. In Figure 4d,e, gray crosses identify locations with non-
 617 significant geopotential anomalies, i.e., with a mean geopotential anomaly calculated over
 618 the 18 selected *reversals* falling within the 10th-90th percentiles interval of the casual
 619 distribution of geopotential mean anomalies. Those locations without gray crosses feature
 620 locations with significant geopotential anomalies, i.e., with a mean geopotential which is
 621 either <10th or >90th percentile of the casual distribution of geopotential mean anomalies.

622

623 Appendix B: Significance analysis of Figure 7

624 Figure 7 reports the difference between the averages of two pools of salinity fields from the
 625 CMEMS Arctic Ocean Reanalysis. The statistical significance of this difference is examined
 626 at each location by performing a non-parametric test (Mann-Whitney-Wilcoxon) on the two
 627 pools defining the two averages, to verify if they come from the same distribution at the 99%
 628 confidence level. Locations whose differences are associated to non-significantly different
 629 pools are marked in gray.

630

631 Appendix C: Calculation of the Cumulative Net Onshore Displacement (X_{Ek}) reported in
 632 Figure 8

633 X_{Ek} is calculated using the following formula, from Cushman-Roisin and Beckers (2011):

634

$$X_{Ek} = \frac{I}{f}$$

635 where f is the coriolis parameter and I is the *wind impulse*, represented as:

$$I \simeq \frac{1}{\rho_0 H} \int_{event} \tau_y dt$$

636 where ρ_0 is the initial density (here set to 1027.85 Kg/m³), H the depth of the Ekman layer
 637 and τ_y the daily meridional wind stress average over A1 (from ERA5 data). H is estimated
 638 as the theoretical Ekman layer depth:

$$H = \sqrt{2K_m/|f|}$$

639

640 where K_m is the turbulent diffusivity, assumed to be $0.1 \text{ m}^2/\text{s}$ and f the Coriolis parameter. At
641 78.8°N , d_{Ek} is equal to 11.8 m .

642 **Authors contributions statement**

643 FDR evolved the initial idea and together with DZ and JC developed the study. AR helped in
644 the interpretation of the dynamics. FC first approached this thematic in his master thesis,
645 under the supervision of FDR, PR, AL and LL. AL provided the *in-situ* atmospheric data from
646 the CCT, while LL provided the marine data from MDI. All analyses were performed by FDR,
647 except for Figure 1, based on the master thesis work of FC. FDR wrote the manuscript with
648 inputs from all authors.

649 **References**

650

651 1. Beszczynska-Möller, Agnieszka, Fahrbach, Eberhard. Rohardt, Gerd, Schauer,
652 Ursula (2012a). Physical oceanography and current meter data from mooring F3-13
653 [Dataset]. PANGAEA. <https://doi.org/10.1594/PANGAEA.800342>

654

655 2. Beszczynska-Möller, A., Fahrbach, E., Schauer, U., & Hansen, E. (2012b). Variability
656 in Atlantic water temperature and transport at the entrance to the Arctic Ocean,
657 1997–2010. *ICES Journal of Marine Science*, 69(5), 852-863.

658

659 3. Beszczynska-Möller, Agnieszka, von Appen, Wilken-Jon, Fahrbach, Eberhard
660 (2015). Physical oceanography and current meter data from mooring F3-14
661 [Dataset]. PANGAEA. <https://doi.org/10.1594/PANGAEA.845648>

662

663 4. Bloshkina, E. V., Pavlov, A. K., & Filchuk, K. (2021). Warming of Atlantic Water in
664 three west Spitsbergen fjords: recent patterns and century-long trends. *Polar*
665 *Research*, 40.

666

667 5. Carmack, E., Polyakov, I., Padman, L., Fer, I., Hunke, E., Hutchings, J., ... & Winsor,
668 P. (2015). Toward quantifying the increasing role of oceanic heat in sea ice loss in
669 the new Arctic. *Bulletin of the American Meteorological Society*, 96(12), 2079-2105.

670

671 6. Chatterjee, S., Raj, R. P., Bertino, L., Skagseth, Ø., Ravichandran, M., &
672 Johannessen, O. M. (2018). Role of Greenland Sea gyre circulation on Atlantic water
673 temperature variability in the Fram Strait. *Geophysical Research Letters*, 45(16),
674 8399-8406.

675

676 7. Chree, C., (1912). Some phenomena of sunspots and of terrestrial magnetism, at
677 Kew observatory. *Philosophical Transactions Royal Society London Series A* 212,
678 75.

679

680 8. Chree, C., (1913). Some phenomena of sunspots and of terrestrial magnetism, II.
681 *Philosophical Transactions Royal Society London Series A* 213, 245.

682

683 9. Chylek, P., Folland, C. K., Lesins, G., Dubey, M. K., & Wang, M. (2009). Arctic air
684 temperature change amplification and the Atlantic Multidecadal Oscillation.
685 *Geophysical Research Letters*, 36(14).

- 686
687 10. CNR – National Research Council of Italy (2022). CTD data set from mooring MDI @
688 35m and 85m (Kongsfjorden) [Dataset]. Italian Arctic Data Center.
689 https://data.iadc.cnr.it/erddap/info/mdi_ctd_timeseries_1/index.html.
690
- 691 11. Comiso, J. C. (2012). Large decadal decline of the Arctic multiyear ice cover. *Journal*
692 *of climate*, 25(4), 1176-1193.
693
- 694 12. CMEMS - Copernicus Marine Service (2022). Arctic Ocean Physics Reanalysis
695 [Dataset]. Copernicus Marine Data Store. <https://doi.org/10.48670/moi-00007>.
696
- 697 13. Cottier, F., Tverberg, V., Inall, M., Svendsen, H., Nilsen, F., & Griffiths, C. (2005).
698 Water mass modification in an Arctic fjord through cross-shelf exchange: The
699 seasonal hydrography of Kongsfjorden, Svalbard. *Journal of Geophysical Research:*
700 *Oceans*, 110(C12).
701
- 702 14. Cottier, F. R., Nilsen, F., Inall, M. E., Gerland, S., Tverberg, V., & Svendsen, H.
703 (2007). Wintertime warming of an Arctic shelf in response to large-scale
704 atmospheric circulation. *Geophysical Research Letters*, 34(10).
705
- 706 15. Cottier, F., Skogseth, R., David, D., and Berge, J. (2019). "Temperature time-series
707 in Svalbard fjords. A contribution from the "Integrated Marine Observatory
708 Partnership(iMOP)", in The e State of Environmental Science in Svalbard report
709 2018, eds E. Orr, G. Hansen, H. Lappalainen, C. Hübner, and H. Lihavainen
710 (Longyearbyen: Svalbard Integrated Arctic Earth Observing System), 108–118.
711
- 712 16. Cottier, F., Berge, J., Griffith, C., Dumont, E., Beaton, J., Vogedes, D. L., UiT The
713 Arctic University of Norway, Scottish Association for Marine Science (2021a).
714 Temperature, salinity, light and fluorescence (CTD) measurements from the
715 Kongsfjorden (Svalbard) marine observatory (mooring) September 2015-August
716 2016 [Dataset]. Norstore. <https://doi.org/10.11582/2021.00061>
717
- 718 17. Cottier, F., Berge, J., Dumont, E., Griffith, C., Beaton, J., Vogedes, D. L., UiT The
719 Arctic University of Norway, Scottish Association for Marine Science (2021b).
720 Temperature, salinity, light and fluorescence (CTD) measurements from the
721 Kongsfjorden (Svalbard) marine observatory (mooring) August 2016-August 2017
722 [Dataset]. Norstore. <https://doi.org/10.11582/2021.00062>

723

724 18. Cottier, F., Berge, J., Dumont, E., Kopec, T. P., Venables, E. J., Vogedes, D. L., UiT
725 The Arctic University of Norway, Scottish Association for Marine Science (2021c).
726 Temperature, salinity, light and fluorescence (CTD) measurements from the
727 Kongsfjorden (Svalbard) marine observatory (mooring) August 2017-August 2018
728 [Dataset]. Norstore. <https://doi.org/10.11582/2021.00065>

729

730 19. Cottier, F., Berge, J., Griffith, C., Dumont, E., Kopec, T. P., Vogedes, D. L., UiT The
731 Arctic University of Norway, Scottish Association for Marine Science (2022a).
732 Temperature, salinity and fluorescence (CTD) measurements from the Kongsfjorden
733 (Svalbard) marine observatory (mooring) June 2006-August 2007 [Dataset].
734 Norstore. <https://doi.org/10.11582/2022.00024>

735

736 20. Cottier, F., Berge, J., Griffith, C., Dumont, E., Kopec, T. P., Vogedes, D. L., UiT The
737 Arctic University of Norway, Scottish Association for Marine Science (2022b).
738 Temperature, salinity, light and fluorescence (CTD) measurements from the
739 Kongsfjorden (Svalbard) marine observatory (mooring) August 2007-August 2008
740 [Dataset]. Norstore. <https://doi.org/10.11582/2022.00025>

741

742 21. Cottier, F., Berge, J., Griffith, C., Dumont, E., Kopec, T. P., Vogedes, D. L., UiT The
743 Arctic University of Norway, Scottish Association for Marine Science (2022c).
744 Temperature, salinity, light and fluorescence (CTD) measurements from the
745 Kongsfjorden (Svalbard) marine observatory (mooring) September 2008-August
746 2009 [Dataset]. Norstore. <https://doi.org/10.11582/2022.00026>

747

748 22. Cottier, F., Berge, J., Griffith, C., Dumont, E., Kopec, T. P., Vogedes, D. L., UiT The
749 Arctic University of Norway, Scottish Association for Marine Science (2022d).
750 Temperature, salinity, light and fluorescence (CTD) measurements from the
751 Kongsfjorden (Svalbard) marine observatory (mooring) September 2009-September
752 2010 [Dataset]. Norstore. <https://doi.org/10.11582/2022.00022>

753

754 23. Cottier, F., Griffith, C., Dumont, E., Kopec, T. P., Vogedes, D. L., UiT The Arctic
755 University of Norway, Scottish Association for Marine Science (2022e). Temperature,
756 salinity, light and fluorescence (CTD) measurements from the Kongsfjorden
757 (Svalbard) marine observatory (mooring) September 2010-September 2011
758 [Dataset]. Norstore. <https://doi.org/10.11582/2022.00023>

759

- 760 24. Cottier, F., Berge, J., Griffith, C., Dumont, E., Kopec, T. P., Vogedes, D. L. (2022f).
761 Temperature, salinity, light and fluorescence (CTD) measurements from the
762 Kongsfjorden (Svalbard) marine observatory (mooring) September 2011-September
763 2012 [Dataset]. Norstore. <https://doi.org/10.11582/2022.00020>
764
- 765 25. Cottier, F., Berge, J., Griffith, C., Dumont, E., Kopec, T. P., Vogedes, D. L., UiT The
766 Arctic University of Norway, Scottish Association for Marine Science (2022g).
767 Temperature, salinity, light and fluorescence (CTD) measurements from the
768 Kongsfjorden (Svalbard) marine observatory (mooring) October 2012-September
769 2013 [Dataset]. Norstore. <https://doi.org/10.11582/2022.00021>
770
- 771 26. Cottier, F., Berge, J., Griffith, C., Dumont, E., Beaton, J., Vogedes, D. L., UiT The
772 Arctic University of Norway, Scottish Association for Marine Science (2022h).
773 Temperature, salinity, light and fluorescence (CTD) measurements from the
774 Kongsfjorden (Svalbard) marine observatory (mooring) September 2013-October
775 2014 [Dataset]. Norstore. <https://doi.org/10.11582/2022.00018>
776
- 777 27. Cottier, F., Berge, J., Griffith, C., Dumont, E., Beaton, J., Vogedes, D. L., Kopec, T.
778 P., UiT The Arctic University of Norway, Scottish Association for Marine Science
779 (2022i). Temperature, salinity, light and fluorescence (CTD) measurements from the
780 Kongsfjorden (Svalbard) marine observatory (mooring) September 2014-September
781 2015 [Dataset]. Norstore. <https://doi.org/10.11582/2022.00019>
782
- 783 28. Curry, J. A., Schramm, J. L., & Ebert, E. E. (1995). Sea ice-albedo climate feedback
784 mechanism. *Journal of Climate*, 8(2), 240-247.
785
- 786 29. Cushman-Roisin, B., & Beckers, J. M. (2011). Introduction to geophysical fluid
787 dynamics: physical and numerical aspects. Academic press.
788
- 789 30. D'Angelo, A., Giglio, F., Miserocchi, S., Sanchez-Vidal, A., Aliani, S., Tesi, T., et al.
790 (2018). Multi-year particle fluxes in Kongsfjorden, Svalbard. *Biogeosciences* 15,
791 5343–5363
792
- 793 31. De Rovere, F., Langone, L., Schroeder, K., Miserocchi, S., Giglio, F., Aliani, S., &
794 Chiggiato, J. (2022). Water Masses Variability in Inner Kongsfjorden (Svalbard)
795 During 2010–2020. *Frontiers in Marine Science*, 9.
796

- 797 32. Duarte, P., Sundfjord, A., Meyer, A., Hudson, S. R., Spreen, G., & Smedsrud, L. H.
798 (2020). Warm Atlantic water explains observed sea ice melt rates north of Svalbard.
799 *Journal of Geophysical Research: Oceans*, 125(8), e2019JC015662.
800
- 801 33. Häkkinen, S., Rhines, P. B., & Worthen, D. L. (2011). Atmospheric blocking and
802 Atlantic multidecadal ocean variability. *Science*, 334(6056), 655-659.
803
- 804 34. Hegseth, E. N., & Tverberg, V. (2013). Effect of Atlantic water inflow on timing of the
805 phytoplankton spring bloom in a high Arctic fjord (Kongsfjorden, Svalbard). *Journal of*
806 *Marine Systems*, 113, 94-105.
807
- 808 35. Helland-Hansen, B., & Nansen, F. (1909). Die jährlichen Schwankungen der
809 Wassermassen im norwegischen Nordmeer in ihrer Beziehung zu den
810 Schwankungen der meteorologischen Verhältnisse, der Ernteerträge und der
811 Fischereiergebnisse in Norwegen. *Internationale Revue der gesamten Hydrobiologie*
812 *und Hydrographie*, 2(3), 337-361.
813
- 814 36. Hersbach, H., Bell, B., Berrisford, P., Biavati, G., Horányi, A., Muñoz Sabater, J.,
815 Nicolas, J., Peubey, C., Radu, R., Rozum, I., Schepers, D., Simmons, A., Soci, C.,
816 Dee, D., Thépaut, J-N. (2023a): ERA5 hourly data on pressure levels from 1940 to
817 present. Copernicus Climate Change Service (C3S) Climate Data Store (CDS), DOI:
818 [10.24381/cds.bd0915c6](https://doi.org/10.24381/cds.bd0915c6)
819
- 820 37. Hersbach, H., Bell, B., Berrisford, P., Biavati, G., Horányi, A., Muñoz Sabater, J.,
821 Nicolas, J., Peubey, C., Radu, R., Rozum, I., Schepers, D., Simmons, A., Soci, C.,
822 Dee, D., Thépaut, J-N. (2023b): ERA5 hourly data on single levels from 1940 to
823 present. Copernicus Climate Change Service (C3S) Climate Data Store (CDS), DOI:
824 [10.24381/cds.adbb2d47](https://doi.org/10.24381/cds.adbb2d47)
825
- 826 38. Holmes, F. A., Kirchner, N., Kuttenukeuler, J., Krüzfeldt, J., & Noormets, R. (2019).
827 Relating ocean temperatures to frontal ablation rates at Svalbard tidewater glaciers:
828 Insights from glacier proximal datasets. *Scientific reports*, 9(1), 1-11.
829
- 830 39. Hop, H., & Wiencke, C. (2019). *The Ecosystem of Kongsfjorden, Svalbard* (pp. 1-20).
831 Springer International Publishing.
832

- 833 40. Inall, M. E., Nilsen, F., Cottier, F. R., & Daae, R. (2015). Shelf/fjord exchange driven
 834 by coastal-trapped waves in the Arctic. *Journal of Geophysical Research: Oceans*,
 835 120(12), 8283-8303.
 836
- 837 41. Ingvaldsen, R. B., Assmann, K. M., Primicerio, R., Fossheim, M., Polyakov, I. V., &
 838 Dolgov, A. V. (2021). Physical manifestations and ecological implications of Arctic
 839 Atlantification. *Nature Reviews Earth & Environment*, 2(12), 874-889.
 840
- 841 42. Jackson, R. H., Straneo, F., & Sutherland, D. A. (2014). Externally forced fluctuations
 842 in ocean temperature at Greenland glaciers in non-summer months. *Nature*
 843 *Geoscience*, 7(7), 503-508.
 844
- 845 43. Klinck, J. M., O'Brien, J. J., & Svendsen, H. (1981). A simple model of fjord and
 846 coastal circulation interaction. *Journal of Physical Oceanography*, 11(12), 1612-1626.
 847
- 848 44. Lind, S., Ingvaldsen, R. B., & Furevik, T. (2018). Arctic warming hotspot in the
 849 northern Barents Sea linked to declining sea-ice import. *Nature climate change*, 8(7),
 850 634-639.
 851
- 852 45. Luckman, A., Benn, D. I., Cottier, F., Bevan, S., Nilsen, F., & Inall, M. (2015). Calving
 853 rates at tidewater glaciers vary strongly with ocean temperature. *Nature*
 854 *communications*, 6(1), 1-7.
 855
- 856 46. Lundesgaard, Ø., Sundfjord, A., Lind, S., Nilsen, F., & Renner, A. H. (2022). Import of
 857 Atlantic Water and sea ice controls the ocean environment in the northern Barents
 858 Sea. *Ocean Science*, 18(5), 1389-1418.
 859
- 860 47. Meredith, M., M. Sommerkorn, S. Cassotta, C. Derksen, A. Ekaykin, A. Hollowed, G.
 861 Kofinas, A. Mackintosh, J. Melbourne-Thomas, M.M.C. Muelbert, G. Ottersen, H.
 862 Pritchard, and E.A.G. Schuur, 2019: Polar Regions. In: IPCC Special Report on the
 863 Ocean and Cryosphere in a Changing Climate [H.-O. Pörtner, D.C. Roberts, V.
 864 Masson-Delmotte, P. Zhai, M. Tignor, E. Poloczanska, K. Mintenbeck, A. Alegría, M.
 865 Nicolai, A. Okem, J. Petzold, B. Rama, N.M. Weyer (eds.)]. Cambridge University
 866 Press, Cambridge, UK and New York, NY, USA, pp. 203–320.
 867 <https://doi.org/10.1017/9781009157964.005>.
 868

- 869 48. Muilwijk, M., Smedsrud, L. H., Ilicak, M., & Drange, H. (2018). Atlantic Water heat
870 transport variability in the 20th century Arctic Ocean from a global ocean model and
871 observations. *Journal of Geophysical Research: Oceans*, 123(11), 8159-8179.
872
- 873 49. Nilsen, F., Gjevik, B., & Schauer, U. (2006). Cooling of the West Spitsbergen
874 Current: Isopycnal diffusion by topographic vorticity waves. *Journal of Geophysical
875 Research: Oceans*, 111(C8).
876
- 877 50. Nilsen, F., Skogseth, R., Vaardal-Lunde, J., & Inall, M. (2016). A simple shelf
878 circulation model: intrusion of Atlantic Water on the West Spitsbergen Shelf. *Journal
879 of Physical Oceanography*, 46(4), 1209-1230.
880
- 881 51. Payne, C. M., & Roesler, C. S. (2019). Characterizing the influence of Atlantic water
882 intrusion on water mass formation and phytoplankton distribution in Kongsfjorden,
883 Svalbard. *Continental Shelf Research*, 191, 104005.
884
- 885 52. Polyakov, I. V., Pnyushkov, A. V., Alkire, M. B., Ashik, I. M., Baumann, T. M.,
886 Carmack, E. C., ... & Yulin, A. (2017). Greater role for Atlantic inflows on sea-ice loss
887 in the Eurasian Basin of the Arctic Ocean. *Science*, 356(6335), 285-291.
888
- 889 53. Raj, R. P., Nilsen, J. Ø., Johannessen, J. A., Furevik, T., Andersen, O. B., & Bertino,
890 L. (2018). Quantifying Atlantic Water transport to the Nordic Seas by remote sensing.
891 *Remote Sensing of Environment*, 216, 758-769.
892
- 893 54. Richter-Menge, J., & Druckenmiller, M. L. (2020). State of the climate in 2019. *Arctic*,
894 101(8), S239-S286.
895
- 896 55. Rogers, J. C., Yang, L., & Li, L. (2005). The role of Fram Strait winter cyclones on
897 sea ice flux and on Spitsbergen air temperatures. *Geophysical Research Letters*,
898 32(6).
899
- 900 56. Ruggieri, P., Alvarez-Castro, M. C., Athanasiadis, P., Bellucci, A., Materia, S., &
901 Gualdi, S. (2020). North Atlantic circulation regimes and heat transport by synoptic
902 eddies. *Journal of Climate*, 33(11), 4769-4785.
903
- 904 57. Serreze, M. C., & Barry, R. G. (2011). Processes and impacts of Arctic amplification:
905 A research synthesis. *Global and planetary change*, 77(1-2), 85-96.

906

907 58. Singh, Y. P. (2006). Statistical considerations in superposed epoch analysis and its
908 applications in space research. *Journal of atmospheric and solar-terrestrial physics*,
909 68(7), 803-813.

910

911 59. Skogseth, R., & Ellingsen, P. G. (2019a). Mooring data from the Isfjorden Mouth -
912 South (I-S) during 9 Sep 2010 to 3 Sep 2011 [Dataset]. Norwegian Polar Institute.
913 <https://doi.org/10.21334/npolar.2019.b0e473c4>

914

915 60. Skogseth, R., & Ellingsen, P. G. (2019b). Mooring data from the Isfjorden Mouth -
916 South (I-S) during 8 Sep 2011 to 3 Sep 2012 [Dataset]. Norwegian Polar Institute.
917 <https://doi.org/10.21334/npolar.2019.2be7bdee>

918

919 61. Skogseth, R., & Ellingsen, P. G. (2019c). Mooring data from the Isfjorden Mouth -
920 South (I-S) during 6 Sep 2012 to 28 Aug 2013 [Dataset]. Norwegian Polar Institute.
921 <https://doi.org/10.21334/npolar.2019.a247e9a9>

922

923 62. Skogseth, R., & Ellingsen, P. G. (2019d). Mooring data from the Isfjorden Mouth -
924 South (I-S) during 2 Sep 2013 to 26 Aug 2014 [Dataset]. Norwegian Polar Institute.
925 <https://doi.org/10.21334/npolar.2019.6813ce6d>

926

927 63. Skogseth, R., & Ellingsen, P. G. (2019e). Mooring data from the Isfjorden Mouth -
928 South (I-S) during 31 Aug 2014 to 24 Aug 2015 [Dataset]. Norwegian Polar Institute.
929 <https://doi.org/10.21334/npolar.2019.11b7e849>

930

931 64. Skogseth, R., & Ellingsen, P. G. (2019f). Mooring data from the Isfjorden Mouth -
932 South (I-S) during 31 Aug 2015 to 12 Aug 2016 [Dataset]. Norwegian Polar Institute.
933 <https://doi.org/10.21334/npolar.2019.21838303>

934

935 65. Skogseth, R., & Ellingsen, P. G. (2019g). Mooring data from the Isfjorden Mouth -
936 South (I-S) during 19 Aug 2016 to 2 Oct 2017 [Dataset]. Norwegian Polar Institute.
937 <https://doi.org/10.21334/npolar.2019.cd7a2f7c>

938

939 66. Skogseth, R., & Ellingsen, P. G. (2019h). Mooring data from the Isfjorden Mouth -
940 South (I-S) during 5 Oct 2017 to 25 Aug 2018 [Dataset]. Norwegian Polar Institute.
941 <https://doi.org/10.21334/npolar.2019.54dcd0c9>

942

- 943 67. Skogseth, R., Olivier, L. L., Nilsen, F., Falck, E., Fraser, N., Tverberg, V., ... & Falk-
 944 Petersen, S. (2020). Variability and decadal trends in the Isfjorden (Svalbard) ocean
 945 climate and circulation—An indicator for climate change in the European Arctic.
 946 *Progress in Oceanography*, 187, 102394.
- 947
- 948 68. Stigebrandt, A. (1981). A mechanism governing the estuarine circulation in deep,
 949 strongly stratified fjords. *Estuarine, Coastal and Shelf Science*, 13(2), 197-211.
- 950
- 951 69. Straneo, F., Hamilton, G. S., Sutherland, D. A., Stearns, L. A., Davidson, F., Hammill,
 952 M. O., ... & Rosing-Asvid, A. (2010). Rapid circulation of warm subtropical waters in a
 953 major glacial fjord in East Greenland. *Nature Geoscience*, 3(3), 182-186.
- 954
- 955 70. Strzelewicz, A., Przyborska, A., & Walczowski, W. (2022). Increased presence of
 956 Atlantic Water on the shelf south-west of Spitsbergen with implications for the Arctic
 957 fjord Hornsund. *Progress in Oceanography*, 200, 102714.
- 958
- 959 71. Svendsen, H. (1980). Exchange processes above sill level between fjords and
 960 coastal water. In *Fjord oceanography* (pp. 355-361). Springer, Boston, MA.
- 961
- 962 72. Svendsen, H., Beszczynska-Møller, A., Hagen, J. O., Lefauconnier, B., Tverberg, V.,
 963 Gerland, S., ... & Wiencke, C. (2002). The physical environment of Kongsfjorden—
 964 Krossfjorden, an Arctic fjord system in Svalbard. *Polar research*, 21(1), 133-166.
- 965
- 966 73. Teigen, S. H., Nilsen, F., & Gjevik, B. (2010). Barotropic instability in the West
 967 Spitsbergen Current. *Journal of Geophysical Research: Oceans*, 115(C7).
- 968
- 969 74. Teigen, S. H., Nilsen, F., Skogseth, R., Gjevik, B., & Beszczynska-Møller, A. (2011).
 970 Baroclinic instability in the West Spitsbergen current. *Journal of Geophysical*
 971 *Research: Oceans*, 116(C7).
- 972
- 973 75. Tverberg, V., Skogseth, R., Cottier, F., Sundfjord, A., Walczowski, W., Inall, M. E., ...
 974 & Nilsen, F. (2019). The Kongsfjorden transect: seasonal and inter-annual variability
 975 in hydrography. In *The Ecosystem of Kongsfjorden, Svalbard* (pp. 49-104). Springer,
 976 Cham.
- 977
- 978 76. Vihtakari, M. (2020). PlotSvalbard: PlotSvalbard - Plot research data from Svalbard
 979 on maps. R package version 0.9.2. <https://github.com/MikkoVihtakari/PlotSvalbard>

- 980
981 77. Vihtakari, M., Welcker, J., Moe, B., Chastel, O., Tartu, S., Hop, H., ... & Gabrielsen,
982 G. W. (2018). Black-legged kittiwakes as messengers of Atlantification in the Arctic.
983 *Scientific Reports*, 8(1), 1-11.
- 984
985 78. von Appen, Wilken-Jon; Beszczynska-Möller, Agnieszka; Fahrbach, Eberhard
986 (2015): Physical oceanography and current meter data from mooring F3-15
987 [Dataset]. PANGAEA <https://doi.org/10.1594/PANGAEA.853902>
988
- 989 79. von Appen, Wilken-Jon; Latarius, Katrin; Kanzow, Torsten (2017): Physical
990 oceanography and current meter data from mooring F3-16 [dataset]. PANGAEA.
991 <https://doi.org/10.1594/PANGAEA.870842>
992
- 993 80. Walczowski, W., & Piechura, J. (2011). Influence of the West Spitsbergen Current on
994 the local climate. *International journal of climatology*, 31(7), 1088-1093.
995
- 996 81. Wang, Q., Wekerle, C., Wang, X., Danilov, S., Koldunov, N., Sein, D., ... & Jung, T.
997 (2020). Intensification of the Atlantic Water supply to the Arctic Ocean through Fram
998 Strait induced by Arctic sea ice decline. *Geophysical Research Letters*, 47(3),
999 e2019GL086682.
- 1000
1001 82. Zahn, M., Akperov, M., Rinke, A., Feser, F., & Mokhov, I. I. (2018). Trends of cyclone
1002 characteristics in the Arctic and their patterns from different reanalysis data. *Journal*
1003 *of Geophysical Research: Atmospheres*, 123(5), 2737-2751.